ACADEMIC PRESS

Available online at www.sciencedirect.com

SCIENCE DIRECT®

Journal of Sound and Vibration 271 (2004) 725–756

JOURNAL OF SOUND AND VIBRATION

www.elsevier.com/locate/jsvi

Vibration of rotating disk/spindle systems with flexible housing/stator assemblies

Jr-Yi Shen[a], Chaw-Wu Tseng[b], I.Y. Shen[c,*]

[a] *Hitachi Global Storage Technologies, San Jose, CA 94065, USA*

[b] *Western Digital Corporation, San Jose, CA 95138, USA*

[c] *Department of Mechanical Engineering, University of Washington, Box 352600, Seattle, WA 98195-2600, USA*

Received 4 March 2002; accepted 4 April 2003

Abstract

The subject of study in this paper is a rotating spindle carrying multiple flexible disks mounted on a flexible housing/stator assembly through ball bearings or hydrodynamic bearings. The disk/spindle system is subjected to prescribed force excitations, and the housing/stator assembly is subjected to prescribed linear and angular base excitations. This paper has two specific goals. The first goal is to derive linearized equations of motion governing free and forced vibration of the spindle/housing system using a Lagrangian formulation. The second goal is to verify the mathematical model through calibrated experiments. Theoretical predictions of natural frequencies agree well with experimental measurements within 5% of difference for spindle motors using ball bearings. Numerical simulations on spindle motors with hydrodynamic bearings indicate that base flexibility could lead to significant spindle vibration.

1. Introduction

For the past decade, the data storage industry has continued to enhance the capacity and performance of computer hard disk drives (HDD) by increasing the track density and spin speed. As an example, next-generation disk drives will adopt DC spindle motors with spin speeds of 20,000 r.p.m. to reduce data access time. In addition, magnetic disks will have a track density around 100,000 tracks per radial inch to enhance storage capacity and to reduce material costs. The high spin speed implies substantial excitations from the surrounding air, bearing defects, and motor electromagnetic forces. The high track density implies that tiny spindle vibration could

*Corresponding author. Tel.: +1-206-543-5718; fax: +1-206-685-8047.
E-mail address: ishen@u.washington.edu (I.Y. Shen).

0022-460X/03/$ - see front matter
doi:10.1016/S0022-460X(03)00413-9

cause significant read/write errors. For example, allowable radial vibration amplitude for disk drives with 100,000 tracks per inch density will be around 25 nm. To qualify for commercial use, these advanced disk drives will need to meet extremely tight shock and vibration specifications. Preliminary experimental results and numerical simulations have indicated that flexibility of HDD's stationary components, such as housings and stators, will significantly affect the natural frequencies and increase the amplitude of disk drive spindles. Therefore, improper design of these stationary components could degrade performance of future advanced disk drives resulting in disqualification.

For the past 10 years, vibration research on disk drive spindle systems primarily assumes that the stationary part is rigid. For example, Shen and Ku [1] developed a mathematical model to study free vibration of a rotating hub that is supported by ball bearings and carries multiple flexible disks. They also verified the predictions through calibrated experiments. Later, Shen [2] augmented the model in Ref. [1] to predict forced vibration of the rotating disk/spindle system. Lee [3,4] and his fellow researchers applied assumed mode methods to study vibration response of rotors carrying multiple flexible disks. Parker and Sathe [5–7] analyzed vibration of a flexible spindle carrying flexible disks using extended operators. Jia [8] used the method of substructure synthesis to consider vibration of multi-span Timosheno shafts carrying multiple disks. Lim [9] developed a finite element method to predict response of rotating disk/spindle systems. Deeyiengyang and Ono [10] and Yang et al. [11] studied the response of a rotating disk/spindle system excited by ball bearing defects. Deeyiengyang and Ono [12] also developed a squeeze-film damper to suppress vibration of disk/spindle systems. Jintanawan et al. [13–15] studied vibration of rotating disk/spindle systems with hydrodynamic bearings. In all these studies, the housing is always assumed rigid and the effects of housing/stator flexibility are neglected. As a result, the HDD industry resorts to trial-and-error approach, which is very expensive and time-consuming given short design cycles of the industry.

In contrast, the steam and gas turbine industry recognized the importance of housing flexibility as early as 1975 [16]. As rotary machines become faster and lighter, the housing flexibility can affect rotor performance considerably. For the past 25 years, housing flexibility has been modeled through use of lumped spring–mass systems [16–19] or finite element methods [20]. Also, housing flexibility has been extracted experimentally [21–23]. Unfortunately, these research results cannot be applied directly to HDD design, because the results are for turbines with slender rotors and heavy disks. In HDD applications, the aspect ratio is just the opposite; the spindle is very short and the disks are very flexible. Therefore, HDD spindles present totally different dynamic characteristics.

To study the effects of housing/stator flexibility on rotating disk/spindle systems, there are three major challenges to overcome. First, the housing is not axisymmetric. Existing HDD disk/spindle models all assume axisymmetry [1–15]. Moreover, existing studies on asymmetry are limited to stationary disk/spindle systems [24–27]. Effects of asymmetry on rotating disk/spindle systems remain open. The second challenge is mode coupling. The presence of the flexible housing will couple spindle modes with deformation of the housing/stator assembly. This is a phenomenon that existing models [1–15] cannot predict. The third challenge is the complexity of housing geometry and dynamics. The housing/stator assembly cannot be modelled as a simple structural element, such as a beam or plate. Integration of finite element formulations with existing models of rotating disk/spindle systems is necessary.

Motivated by the industrial needs and the academic challenges, this paper is to develop a mathematical model predicting free and forced vibration of rotating disk/spindle systems mounted onto flexible housing/stator assembly. The mathematical model developed in this paper will be valid for spindles shown in Figs. 1 and 2, which are known as fixed-shaft design. The design has three main components: rotating part, stationary part, and bearings. The rotating part consists of a hub and multiple disks. The hub is relatively massive and can be assumed to be rigid. In contrast, the disks are thin and flexible. The stationary part is assembly of a shaft (stator) and housing. The stationary shaft can be cantilevered (i.e., without top attachment in Fig. 1) or fixed at both ends (i.e., with top attachment in Fig. 2). The bearings can be ball bearings or hydrodynamic bearings. Finally, the spindle is subjected to external force and base excitations. The force excitations can be prescribed concentrated or distributed loads applied to either the rotating part or the stationary part. The base excitations can be prescribed rigid-body translation and rotation applied to the stationary part.

In this paper, vibration of the housing/stator is modelled through normal vibration modes. Vibration of the rotating disks and spindle is formulated in terms of axial and rocking motion of the spindle as well as vibration modes of each disk. The bearings are modelled through 5×5 stiffness and damping matrices. Application of Lagrange equations leads to the equations of motion. To verify the mathematical model, the authors measured natural frequencies of a ball-bearing spindle with four different housing configurations. The authors also numerically simulate

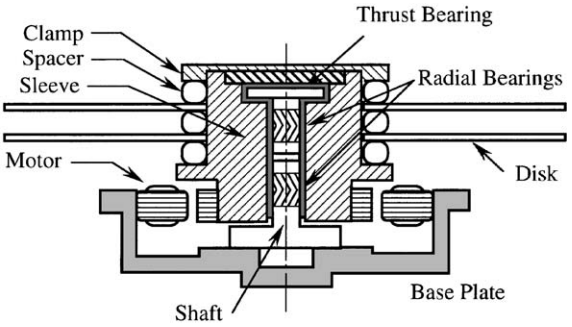

Fig. 1. Fixed-shaft design without top attachment.

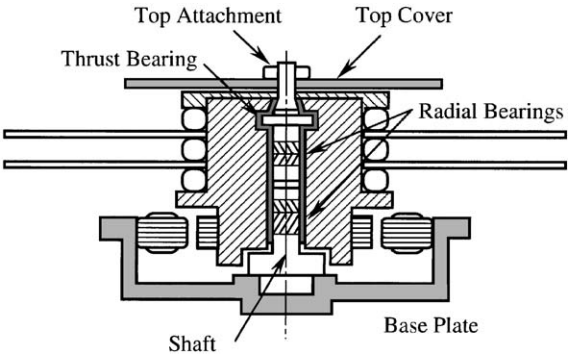

Fig. 2. Fixed-shaft design with top attachment.

frequency response functions of spindle motors with hydrodynamic bearings mounted on three different housing configurations.

2. Formulation of the stationary part

The stationary part is modelled as an elastic structure with arbitrary shapes. In addition, the stationary part is mounted onto a rigid shaker table, which provides linear and angular base excitations. Let O be a convenient reference point on the stationary part. With O being the origin, one can define an inertia frame XYZ with XY plane being parallel to the shaker table initially. In addition, the XYZ frame has unit vectors $\mathbf{I}$, $\mathbf{J}$, and $\mathbf{K}$.

The stationary part is first subjected to a rigid-body base excitation in the form of prescribed three-dimensional infinitesimal rotations γ_x, γ_y, and γ_z as shown in Fig. 3. After the rigid-body rotations, the stationary part rotates to a new set of co-ordinates $\hat{X}\hat{Y}\hat{Z}$ with unit vectors $\hat{\mathbf{I}}$, $\hat{\mathbf{J}}$, and $\hat{\mathbf{K}}$. For convenience, the co-ordinates $\hat{X}\hat{Y}\hat{Z}$ will be termed shaker frame in this paper. For infinitesimal rotation, the co-ordinate systems XYZ and $\hat{X}\hat{Y}\hat{Z}$ are related through

$$\begin{pmatrix} \hat{\mathbf{I}} \\ \hat{\mathbf{J}} \\ \hat{\mathbf{K}} \end{pmatrix} \approx \begin{bmatrix} 1 & \gamma_z & -\gamma_y \\ -\gamma_z & 1 & \gamma_x \\ \gamma_y & -\gamma_x & 1 \end{bmatrix} \begin{pmatrix} \mathbf{I} \\ \mathbf{J} \\ \mathbf{K} \end{pmatrix}. \tag{1}$$

Moreover, the angular velocity and acceleration of the shaker frame are

$$\boldsymbol{\omega}_{\hat{X}\hat{Y}\hat{Z}} \approx \dot{\gamma}_x \hat{\mathbf{I}} + \dot{\gamma}_y \hat{\mathbf{J}} + \dot{\gamma}_z \hat{\mathbf{K}} \tag{2}$$

and

$$\dot{\boldsymbol{\omega}}_{\hat{X}\hat{Y}\hat{Z}} \approx \ddot{\gamma}_x \hat{\mathbf{I}} + \ddot{\gamma}_y \hat{\mathbf{J}} + \ddot{\gamma}_z \hat{\mathbf{K}}. \tag{3}$$

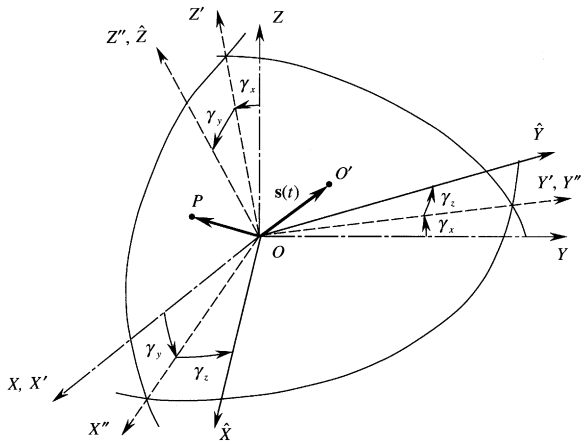

Fig. 3. Prescribed rotational base excitation $(\gamma_x, \gamma_y, \gamma_z)$ and linear base excitation $\mathbf{s}(t)$.

In addition to the angular base excitation, the stationary part is also subjected to a linear base excitation $\mathbf{s}(t)$ defined as

$$\mathbf{s}(t) \equiv s_x(t)\mathbf{I} + s_y(t)\mathbf{J} + s_z(t)\mathbf{K}. \tag{4}$$

As a result of the linear base excitation, the origin O moves to O' as shown in Fig. 3.

Now consider an arbitrary point P on the stationary part. The motion of point P consists of two parts. One is the rigid-body motion consistent with the base excitations. The other is an elastic deformation superimposed on the rigid-body motion. When the base excitation is absent, the location of P is defined through the position vector

$$\mathbf{r} \equiv r_x\mathbf{I} + r_y\mathbf{J} + r_z\mathbf{K}. \tag{5}$$

With the angular base excitations, the rigid-body rotation causes point P to move to its new position $\hat{\mathbf{r}}$ defined as

$$\hat{\mathbf{r}} \equiv r_x\hat{\mathbf{I}} + r_y\hat{\mathbf{J}} + r_z\hat{\mathbf{K}}. \tag{6}$$

Therefore, the rigid-body displacement for point P is

$$\mathbf{R}_{P'} \equiv \mathbf{s}(t) + (\hat{\mathbf{r}} - \mathbf{r}), \tag{7}$$

which consists of infinitesimal translation and rotation.

Let $\mathbf{W}(\hat{\mathbf{r}}, t)$ be the elastic deformation of the stationary part at point P. The elastic deformation $\mathbf{W}(\hat{\mathbf{r}}, t)$ can be approximated in terms of n_b vibration modes of the stationary part as

$$\mathbf{W}(\hat{\mathbf{r}}, t) \equiv \sum_{n=1}^{n_b} \mathbf{W}_n(\hat{\mathbf{r}})q_n(t). \tag{8}$$

where

$$\mathbf{W}_n(\hat{\mathbf{r}}) \equiv W_{xn}(\hat{\mathbf{r}})\hat{\mathbf{I}} + W_{yn}(\hat{\mathbf{r}})\hat{\mathbf{J}} + W_{zn}(\hat{\mathbf{r}})\hat{\mathbf{K}} \tag{9}$$

is the nth vibration mode shape of the stationary part and $q_n(t)$ is the corresponding generalized co-ordinate. In addition, the mode shapes satisfy the orthonormality condition

$$\int \mathbf{W}_m(\hat{\mathbf{r}}) \cdot \mathbf{W}_n(\hat{\mathbf{r}})\,\mathrm{d}m = \delta_{mn} \tag{10}$$

and

$$\int V_b[\mathbf{W}_m(\hat{\mathbf{r}}), \mathbf{W}_n(\hat{\mathbf{r}})]\,\mathrm{d}V = \omega_{bn}^2\delta_{mn}, \tag{11}$$

where δ_{mn} is the Kronecker delta, ω_{bn} is the natural frequency of the nth vibration mode of the stationary part, and $V_b[\cdot]$ is the potential energy operator for the stationary part.

With the rigid-body motion $\mathbf{R}_{P'}$ and elastic deformation $\mathbf{W}(\hat{\mathbf{r}}, t)$, the displacement of P is

$$\mathbf{R}_P \equiv \mathbf{s}(t) + (\hat{\mathbf{r}} - \mathbf{r}) + \mathbf{W}(\hat{\mathbf{r}}, t). \tag{12}$$

As a result, the velocity of point P is

$$\dot{\mathbf{R}}_P = \dot{\mathbf{s}} + \boldsymbol{\omega}_{\hat{X}\hat{Y}\hat{Z}} \times \hat{\mathbf{r}} + \sum_{n=1}^{n_b} \mathbf{W}_n(\hat{\mathbf{r}})\dot{q}_n(t) + \sum_{n=1}^{n_b} [\boldsymbol{\omega}_{\hat{X}\hat{Y}\hat{Z}} \times \mathbf{W}_n(\hat{\mathbf{r}})]q_n(t), \tag{13}$$

where Eq. (8) has been used. If higher order terms are neglected, the kinetic energy of the stationary part becomes

$$T_B = \frac{1}{2}\int (\dot{\mathbf{s}}\cdot\dot{\mathbf{s}})\,\mathrm{d}m + \frac{1}{2}\int \left(\boldsymbol{\omega}_{\hat{X}\hat{Y}\hat{Z}}\times\hat{\mathbf{r}}\right)\cdot\left(\boldsymbol{\omega}_{\hat{X}\hat{Y}\hat{Z}}\times\hat{\mathbf{r}}\right)\mathrm{d}m + \frac{1}{2}\int\left[\sum_{n=1}^{n_b}\mathbf{W}_n(\hat{\mathbf{r}})\dot{q}_n\right]\cdot\left[\sum_{n=1}^{n_b}\mathbf{W}_n(\hat{\mathbf{r}})\dot{q}_n\right]\mathrm{d}m + \int\dot{\mathbf{s}}\cdot\left(\boldsymbol{\omega}_{\hat{X}\hat{Y}\hat{Z}}\times\hat{\mathbf{r}}\right)\mathrm{d}m + \int\dot{\mathbf{s}}\cdot\left[\sum_{n=1}^{n_b}\mathbf{W}_n(\hat{\mathbf{r}})\dot{q}_n\right]\mathrm{d}m + \int\left(\boldsymbol{\omega}_{\hat{X}\hat{Y}\hat{Z}}\times\hat{\mathbf{r}}\right)\cdot\left[\sum_{n=1}^{n_b}\mathbf{W}_n(\hat{\mathbf{r}})\dot{q}_n\right]\mathrm{d}m. \tag{14}$$

Let us define

$$\mathbf{J}_{s1} \equiv \int \hat{\mathbf{r}}\,\mathrm{d}m, \quad \mathbf{J}_{an} \equiv \int \mathbf{W}_n(\hat{\mathbf{r}})\,\mathrm{d}m, \quad \mathbf{J}_{bn} \equiv \int \hat{\mathbf{r}}\times\mathbf{W}_n(\hat{\mathbf{r}})\,\mathrm{d}m. \tag{15-17}$$

Rearranging Eq. (14) results in

$$T_B = \frac{1}{2}m_B(\dot{s}_x^2+\dot{s}_y^2+\dot{s}_z^2) + \frac{1}{2}\boldsymbol{\omega}_{\hat{X}\hat{Y}\hat{Z}}\cdot\mathbf{I}_B\cdot\boldsymbol{\omega}_{\hat{X}\hat{Y}\hat{Z}} + \frac{1}{2}\sum_{n=1}^{n_b}\dot{q}_n^2 + \sum_{n=1}^{n_b}(\dot{\mathbf{s}}\cdot\mathbf{J}_{an})\dot{q}_n + \sum_{n=1}^{n_b}(\boldsymbol{\omega}_{\hat{X}\hat{Y}\hat{Z}}\cdot\mathbf{J}_{bn})\dot{q}_n + \dot{\mathbf{s}}\cdot\boldsymbol{\omega}_{\hat{X}\hat{Y}\hat{Z}}\times\mathbf{J}_{s1}, \tag{18}$$

where $\mathbf{I}_B$ is the mass moment of inertia tensor of the stationary part relative to the origin O. Finally, the potential energy of the stationary part is

$$V_B = \frac{1}{2}\int V_b[\mathbf{W},\mathbf{W}]\,\mathrm{d}V = \frac{1}{2}\sum_{n=1}^{n_b}\omega_{bn}^2 q_n^2(t). \tag{19}$$

3. Formulation of the rotating part

The rotating part consists of a rigid hub carrying N flexible disks. Consider the ith disk, where i can range from 1 to N. The ith disk has density ρ_i, Young's modulus E_i, the Poisson ratio v_i, thickness h_i, and flexural rigidity D_i. In addition, the disk/spindle assembly spins about its centerline with constant angular velocity ω_3. According to Ref. [1], the motion of the rotating part can be described in terms of rigid-body translation (R_x, R_y, R_z) and rocking of the spindle (θ_x, θ_y) as well as vibration modes of each disk $q_{mn}^{(i)}$. They are summarized as follows.

To describe the spindle motion, let G be the centroid of the rotating part. Let us also define G' as a point on the shaker frame whose position vector is

$$\mathbf{r}_{G'} = \overrightarrow{OG}' \equiv t_x\hat{\mathbf{I}} + t_y\hat{\mathbf{J}} + t_z\hat{\mathbf{K}}. \tag{20}$$

When the system is subjected to no external excitations and no motion, note that the shaker frame and the inertia frame coincide and so do G and G'. When the external excitations are present, the

centroid G undergoes an absolute rigid-body displacement $\mathbf{R}_G$. In the meantime, G' on the shaker frame experiences a rigid-body motion according to Eq. (7) as

$$\mathbf{R}_{G'} = (s_x + t_z\gamma_y - t_y\gamma_z)\mathbf{I} + (s_y + t_x\gamma_z - t_z\gamma_x)\mathbf{J} + (s_z + t_y\gamma_x - t_x\gamma_y)\mathbf{K}. \tag{21}$$

Therefore, one can describe the spindle translation $\mathbf{R}(t)$ in terms of relative rigid-body displacement of G to G' (see Fig. 4) defined as

$$\mathbf{R}(t) \equiv R_x(t)\mathbf{I} + R_x(t)\mathbf{J} + R_z(t)\mathbf{K} \equiv \mathbf{R}_G - \mathbf{R}_{G'}. \tag{22}$$

The biggest advantage of using $\mathbf{R}(t)$ defined in Eq. (22) is the simplicity of resulting equations of motion, which will be demonstrated later.

To describe spindle rocking, the centerline of the rotating spindle defines the z-axis of a rocking co-ordinate system xyz with unit vectors $\mathbf{i}$, $\mathbf{j}$, and $\mathbf{k}$. In the rocking co-ordinates xyz, the x and y axes are defined through Euler angles θ_x and θ_y as shown in Fig. 5. For infinitesimal rocking,

$$\begin{pmatrix} \mathbf{i} \\ \mathbf{j} \\ \mathbf{k} \end{pmatrix} \approx \begin{bmatrix} 1 & 0 & -\theta_y \\ 0 & 1 & \theta_x \\ \theta_y & -\theta_x & 1 \end{bmatrix} \begin{pmatrix} \mathbf{I} \\ \mathbf{J} \\ \mathbf{K} \end{pmatrix}. \tag{23}$$

Note that each disk will spin relative to the rocking co-ordinates xyz with angular velocity $\omega_3\mathbf{k}$.

Let $\mathbf{w}_i$ be the deflection of the ith disk; therefore

$$\mathbf{w}_i = w_i(r, \beta, t)\mathbf{k}. \tag{24}$$

Moreover, the deflection w_i can be discretized through an eigenfunction expansion,

$$w_i(r, \beta, t) = \sum_{m=0}^{\infty} \sum_{n=-\infty}^{\infty} w_{mn}(r, \beta) q_{mn}^{(i)}(t), \tag{25}$$

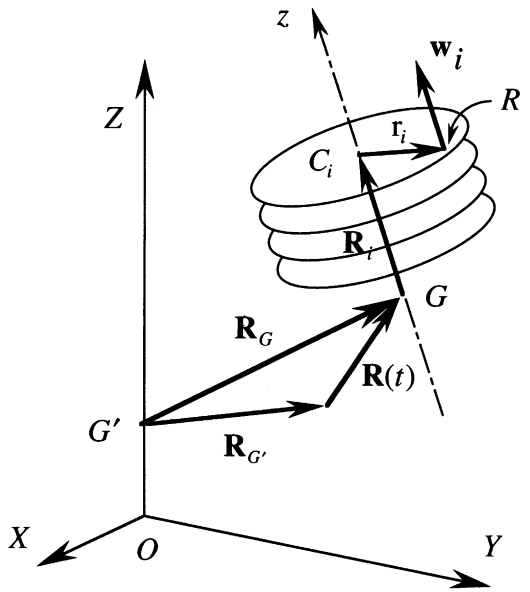

Fig. 4. Translation and rocking of the rotating part.

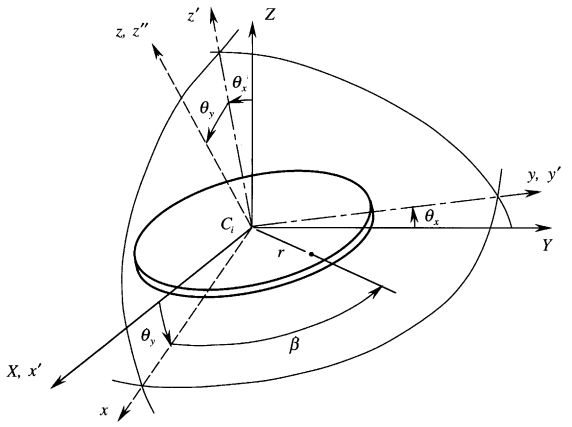

Fig. 5. Euler angles defining the rocking co-ordinates.

where $q_{mn}^{(i)}(t)$ are the generalized co-ordinates and $w_{mn}^{(i)}(r,\beta)$ are the mode shapes of the ith disk with m nodal circles and n nodal diameters. Furthermore, the mode shape $w_{mn}^{(i)}(r,\beta)$ can be expressed explicitly as

$$w_{mn}^{(i)}(r,\beta) = \begin{cases} R_{mn}^{(i)}(r)\cos n\beta, & n \geqslant 0, \\ R_{mn}^{(i)}(r)\sin |n|\beta, & n < 0, \end{cases} \tag{26}$$

under the following orthonormality conditions

$$\int w_{mn}^{(i)} w_{pq}^{(i)}\, \mathrm{d}m_i = I_1^{(i)}\delta_{mp}\delta_{nq} \tag{27}$$

and

$$V_i[w_{mn}^{(i)}, w_{pq}^{(i)}] = I_1^{(i)}[\omega_{mn}^{(i)}]^2\delta_{mp}\delta_{nq}, \tag{28}$$

where $I_1^{(i)}$ is the diametrical mass moment of inertia of the ith disk, $V_i[\cdot]$ is the strain energy operator of the ith elastic disk, and $\omega_{mn}^{(i)}$ are the natural frequency associated with the mode shape $w_{mn}^{(i)}$.

In terms of these generalized co-ordinates R_x, R_y, R_z, θ_x, θ_y, and $q_{mn}^{(i)}$, Shen and Ku [1] derived the kinetic energy of the rotating disk pack up to a quadratic form as

$$\begin{aligned} T_R = {} & \frac{M}{2}[(\dot{R}_x + \dot{s}_x + t_z\dot{\gamma}_y - t_y\dot{\gamma}_z)^2 + (\dot{R}_y + \dot{s}_y + t_x\dot{\gamma}_z - t_z\dot{\gamma}_x)^2 \\ & + (\dot{R}_z + \dot{s}_z + t_y\dot{\gamma}_x - t_x\dot{\gamma}_y)^2] + \frac{1}{2}\bar{I}_1(\dot{\theta}_x^2\cos^2\theta_y + \dot{\theta}_y^2) + \frac{1}{2}\bar{I}_3(\omega_3 + \dot{\theta}_x\sin\theta_y)^2 \\ & + \frac{1}{2}\sum_{i=1}^{N} I_1^{(i)}\left[\sum_{m=0}^{\infty}\sum_{n=-\infty}^{\infty}(\dot{q}_{mn}^{(i)} + n\omega_3 q_{m,-n}^{(i)})^2\right] \end{aligned}$$

$$+\dot{\theta}_x\cos\theta_y\sum_{i=1}^{N} I_1^{(i)}\left[\sum_{m=0}^{\infty} a_m^{(i)}(\dot{q}_{m,-1}^{(i)} - 2\omega_3 q_{m1}^{(i)})\right]$$

$$-\dot{\theta}_y\sum_{i=1}^{N} I_1^{(i)}\left[\sum_{m=0}^{\infty} a_m^{(i)}(\dot{q}_{m1}^{(i)} + 2\omega_3 q_{m,-1}^{(i)})\right]$$

$$+[(\dot{R}_x + \dot{s}_x + t_z\dot{\gamma}_y - t_y\dot{\gamma}_z)\sin\theta_y - (\dot{R}_y + \dot{s}_y + t_x\dot{\gamma}_z - t_z\dot{\gamma}_x)\sin\theta_x\cos\theta_y$$

$$+(\dot{R}_z + \dot{s}_z + t_y\dot{\gamma}_x - t_x\dot{\gamma}_y)\cos\theta_x\cos\theta_y]\sum_{i=1}^{N} I_1^{(i)}\left[\sum_{m=0}^{\infty} b_m^{(i)}\dot{q}_{m0}^{(i)}\right], \tag{29}$$

where $\bar{I}_1$ and $\bar{I}_3$ are transverse and polar mass moments of inertia tensor of the rotating disk/spindle system with respect to the center of mass of the system. Moreover,

$$a_m^{(i)} = \frac{\pi\rho_i h_i}{I_1^{(i)}}\int_{a_i}^{b_i} R_{m1}^{(i)}(r)r^2\,\mathrm{d}r, \tag{30}$$

$$b_m^{(i)} = \frac{2\pi\rho_i h_i}{I_1^{(i)}}\int_{a_i}^{b_i} R_{m0}^{(i)}(r)r\,\mathrm{d}r. \tag{31}$$

Finally, the potential energy of the disk pack can be discretized in terms of the generalized co-ordinates as [1]

$$V_R = \frac{1}{2}\sum_{i=1}^{N} I_1^{(i)}\sum_{m=0}^{\infty}\sum_{n=-\infty}^{\infty}[\omega_{mn}^{(i)}q_{mn}^{(i)}]^2. \tag{32}$$

4. Bearing deformation

The purpose of this section is to derive bearing deformations in terms of the generalized co-ordinates associated with the rotating and stationary parts. Let A and A' be two mating surfaces of a bearing (e.g., inner race and outer race) as shown in Fig. 6(a) and (b). Note that surface A is on the rotating part and surface A' is on the stationary part. When the spindle vibrates, the two bearing surfaces move relative to each other. In addition, the relative motion could be linear or angular.

To determine the bearing deformation, let us define the location and orientation of the bearing surfaces first. When the spindle is at rest and the bearing A is undeformed, let the position of A be

$$\overrightarrow{OA} = p_x\mathbf{I} + p_y\mathbf{J} + p_z\mathbf{K}, \tag{33}$$

where p_x, p_y, and p_z are the Cartesian co-ordinates of bearing A with respect to the origin O; see Fig. 7. Also, the relative position of A to G can be defined as

$$\overrightarrow{GA} = l_x\mathbf{I} + l_y\mathbf{J} + l_z\mathbf{K}. \tag{34}$$

Note that the centroid location $\overrightarrow{OG}$ has been defined in Eq. (20), because G and G' coincide in this case, and so do $\hat{X}\hat{Y}\hat{Z}$ and XYZ. Since $\overrightarrow{OG} + \overrightarrow{GA} = \overrightarrow{OA}$,

$$t_i + l_i = p_i, \quad i = x, y, z. \tag{35}$$

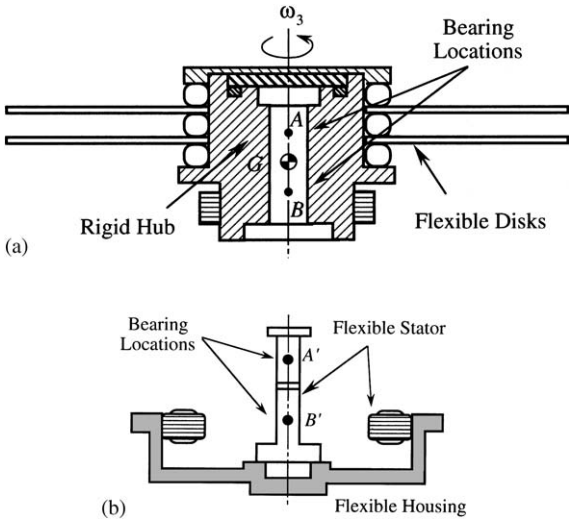

Fig. 6. Mating surfaces A and A' of a bearing; (a) surface A is on the rotating part, and (b) surface A' is on the non-rotating part.

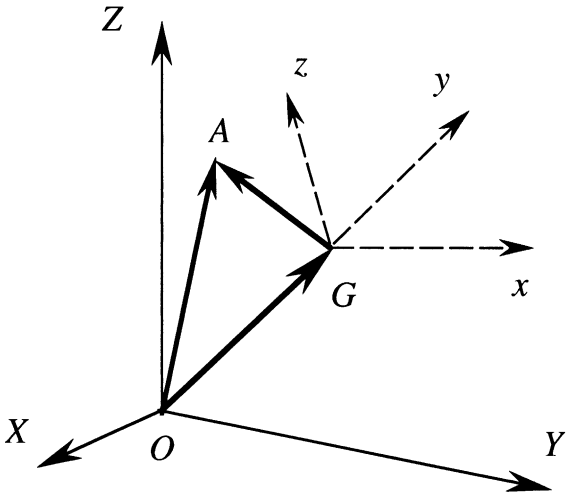

Fig. 7. Position of A and G when the spindle is at rest and bearing is undeformed fixed-shaft design with top attachment.

When the spindle vibrates, the shaker frame $\hat{X}\hat{Y}\hat{Z}$ attached to the stationary part undergoes an infinitesimal rotation from shaker excitation,

$$\hat{\boldsymbol{\gamma}} \approx \gamma_x \hat{\mathbf{I}} + \gamma_y \hat{\mathbf{J}} + \gamma_z \hat{\mathbf{K}}, \tag{36}$$

and the rocking co-ordinate xyz on the rotating part undergoes an infinitesimal rotation

$$\hat{\boldsymbol{\theta}} \approx \theta_x \hat{\mathbf{I}} + \theta_y \hat{\mathbf{J}}. \tag{37}$$

Moreover, the elastic deformation of the stationary part will induce an infinitesimal rigid-body rotation

$$\boldsymbol{\alpha} \equiv \alpha_x \hat{\mathbf{I}} + \alpha_y \hat{\mathbf{J}} + \alpha_z \hat{\mathbf{K}} = \frac{1}{2} \nabla \times \sum_{n=1}^{n_b} \mathbf{W}_n(\hat{\mathbf{r}}_A) q_n, \tag{38}$$

where $\hat{\mathbf{r}}_A$ is the position vector of A in the shaker frame. Or more explicitly,

$$\alpha_x = \frac{1}{2} \sum_{n=1}^{n_b} \left[\frac{\partial W_{zn}}{\partial y} - \frac{\partial W_{yn}}{\partial z} \right]_{\hat{\mathbf{r}}=\hat{\mathbf{r}}_A} q_n \equiv \sum_{n=1}^{n_b} \alpha_{xn} q_n, \tag{39}$$

$$\alpha_y = \frac{1}{2} \sum_{n=1}^{n_b} \left[\frac{\partial W_{xn}}{\partial z} - \frac{\partial W_{zn}}{\partial x} \right]_{\hat{\mathbf{r}}=\hat{\mathbf{r}}_A} q_n \equiv \sum_{n=1}^{n_b} \alpha_{yn} q_n, \tag{40}$$

$$\alpha_z = \frac{1}{2} \sum_{n=1}^{n_b} \left[\frac{\partial W_{yn}}{\partial x} - \frac{\partial W_{xn}}{\partial y} \right]_{\hat{\mathbf{r}}=\hat{\mathbf{r}}_A} q_n \equiv \sum_{n=1}^{n_b} \alpha_{zn} q_n. \tag{41}$$

To determine the linear bearing deformation, let $\mathbf{r}_A$ and $\mathbf{r}_{A'}$ be the position vector of A and A', respectively. Then $\mathbf{r}_A - \mathbf{r}_{A'}$ defines the linear bearing deformation. Note that

$$\mathbf{r}_A = (t_x \mathbf{I} + t_y \mathbf{J} + t_z \mathbf{K}) + \mathbf{R}_G + (l_x \mathbf{i} + l_y \mathbf{j} + l_z \mathbf{k}). \tag{42}$$

Use of Eqs. (1) and (23) transforms $\mathbf{r}_A$ to shaker co-ordinates $\hat{X}\hat{Y}\hat{Z}$ as

$$\mathbf{r}_A = \mathbf{R}_G + (p_x \hat{\mathbf{I}} + p_y \hat{\mathbf{J}} + p_z \hat{\mathbf{K}}) - \hat{\boldsymbol{\gamma}} \times (t_x \hat{\mathbf{I}} + t_y \hat{\mathbf{J}} + t_z \hat{\mathbf{K}}) + (\hat{\boldsymbol{\theta}} - \hat{\boldsymbol{\gamma}}) \times (l_x \hat{\mathbf{I}} + l_y \hat{\mathbf{J}} + l_z \hat{\mathbf{K}}), \tag{43}$$

where Eq. (35) has been used. Similarly,

$$\mathbf{r}_{A'} = \mathbf{s} + (p_x \hat{\mathbf{I}} + p_y \hat{\mathbf{J}} + p_z \hat{\mathbf{K}}) + \sum_{n=1}^{n_b} \mathbf{W}(\hat{\mathbf{r}}_A) q_n(t). \tag{44}$$

Based on Eqs. (43) and (44), the linear bearing deformation is

$$\mathbf{r}_A - \mathbf{r}_{A'} \equiv \Delta_x \hat{\mathbf{I}} + \Delta_y \hat{\mathbf{J}} + \Delta_z \hat{\mathbf{K}}, \tag{45}$$

where

$$\Delta_x \equiv R_x + l_z \theta_y - l_z \gamma_y + l_y \gamma_z - \sum_{n=1}^{n_b} W_{xn}(\hat{\mathbf{r}}_A) q_n, \tag{46}$$

$$\Delta_y \equiv R_y - l_z \theta_x - l_x \gamma_z + l_z \gamma_x - \sum_{n=1}^{n_b} W_{yn}(\hat{\mathbf{r}}_A) q_n \tag{47}$$

and

$$\Delta_z \equiv R_z - l_x \theta_y + l_y \theta_x + l_x \gamma_y - l_y \gamma_x - \sum_{n=1}^{n_b} W_{zn}(\hat{\mathbf{r}}_A) q_n. \tag{48}$$

Note that Eq. (22) has been used to derive Eqs. (46)–(48).

The relative angular displacements of A relative A' about $\hat{X}$ and $\hat{Y}$ axes are simply

$$\xi_x = \theta_x - \gamma_x - \alpha_x \tag{49}$$

and

$$\xi_y = \theta_y - \gamma_y - \alpha_y. \tag{50}$$

5. Vector notation

To keep track of the lengthy derivation, it is beneficial to adopt the following vector notations. Define the vector of generalized coordinates as

$$\mathbf{q} = [\mathbf{d}^{\mathrm{T}}, \mathbf{q}_{00}^{\mathrm{T}}, \mathbf{q}_{01}^{\mathrm{T}}, \mathbf{q}_{0,-1}^{\mathrm{T}}, \mathbf{q}_B^{\mathrm{T}}]^{\mathrm{T}}. \tag{51}$$

In Eq. (51),

$$\mathbf{d} \equiv [R_x, R_y, R_z, \theta_x, \theta_y]^{\mathrm{T}} \tag{52}$$

is the vector describing the translation and rocking of the rotating disk pack,

$$\mathbf{q}_{00} \equiv [q_{00}^{(1)}, q_{00}^{(2)}, \ldots, q_{00}^{(N)}]^{\mathrm{T}} \tag{53}$$

defines the generalized co-ordinates of $(0,0)$ disk mode for each disk. Moreover,

$$\mathbf{q}_{01} = [q_{01}^{(1)}, q_{01}^{(2)}, \ldots, q_{01}^{(N)}]^{\mathrm{T}} \tag{54}$$

and

$$\mathbf{q}_{0,-1} = [q_{0,-1}^{(1)}, q_{0,-1}^{(2)} \quad \ldots, q_{0,-1}^{(N)}]^{\mathrm{T}} \tag{55}$$

define the generalized co-ordinates of $(0,1)$ disk modes, respectively. Finally,

$$\mathbf{q}_B = [q_1, q_2, \ldots, q_{n_b}]^{\mathrm{T}} \tag{56}$$

defines the generalized co-ordinates of the stationary part. Aside from generalized co-ordinates, let us define the vector of shaker excitations as

$$\mathbf{f}_s = [s_x, s_y, s_z, \gamma_x, \gamma_y, \gamma_z]^{\mathrm{T}}. \tag{57}$$

With the vector notation, the linear and angular bearing deformations from Eqs. (46) to (50) can be rewritten as

$$\mathbf{\Delta}_b \equiv [\Delta_x, \Delta_y, \Delta_z, \xi_x, \xi_y]^{\mathrm{T}} = \mathbf{B}_b\mathbf{q} + \mathbf{h}_b\mathbf{f}_s, \tag{58}$$

where

$$\mathbf{B}_b = \begin{bmatrix} 1 & 0 & 0 & 0 & l_z & \mathbf{0} & \mathbf{0} & \mathbf{0} & -\mathbf{W}_x \\ 0 & 1 & 0 & -l_z & 0 & \mathbf{0} & \mathbf{0} & \mathbf{0} & -\mathbf{W}_y \\ 0 & 0 & 1 & l_y & -l_x & \mathbf{0} & \mathbf{0} & \mathbf{0} & -\mathbf{W}_z \\ 0 & 0 & 0 & 1 & 0 & \mathbf{0} & \mathbf{0} & \mathbf{0} & -\boldsymbol{\alpha}_x \\ 0 & 0 & 0 & 0 & 1 & \mathbf{0} & \mathbf{0} & \mathbf{0} & -\boldsymbol{\alpha}_y \end{bmatrix}, \tag{59}$$

$$\mathbf{h}_b = \begin{bmatrix} 0 & 0 & 0 & 0 & -l_z & l_y \\ 0 & 0 & 0 & l_z & 0 & -l_x \\ 0 & 0 & 0 & -l_y & l_x & 0 \\ 0 & 0 & 0 & -1 & 0 & 0 \\ 0 & 0 & 0 & 0 & -1 & 0 \end{bmatrix}, \tag{60}$$

with

$$\mathbf{W}_x \equiv [W_{x1}(\hat{\mathbf{r}}_A), W_{x2}(\hat{\mathbf{r}}_A), \ldots, W_{xn_b}(\hat{\mathbf{r}}_A)], \tag{61}$$

$$\mathbf{W}_y \equiv [W_{y1}(\hat{\mathbf{r}}_A), W_{y2}(\hat{\mathbf{r}}_A), \ldots, W_{yn_b}(\hat{\mathbf{r}}_A)], \tag{62}$$

$$\mathbf{W}_z \equiv [W_{z1}(\hat{\mathbf{r}}_A), W_{z2}(\hat{\mathbf{r}}_A), \ldots, W_{zn_b}(\hat{\mathbf{r}}_A)], \tag{63}$$

$$\boldsymbol{\alpha}_x \equiv [\alpha_{x1}, \alpha_{x2}, \ldots, \alpha_{xn_b}] \tag{64}$$

and

$$\boldsymbol{\alpha}_y \equiv [\alpha_{y1}, \alpha_{y2}, \ldots, \alpha_{yn_b}]. \tag{65}$$

Also, the following matrices and vectors turn out to be useful in later derivation

$$\boldsymbol{\omega}_{00} = \mathrm{diag}[(\omega_{00}^{(1)})^2, (\omega_{00}^{(2)})^2, \ldots, (\omega_{00}^{(N)})^2], \tag{66}$$

$$\boldsymbol{\omega}_{01} = \mathrm{diag}[(\omega_{01}^{(1)})^2, (\omega_{01}^{(2)})^2, \ldots, (\omega_{01}^{(N)})^2], \tag{67}$$

$$\boldsymbol{\omega}_B = \mathrm{diag}[\omega_{b1}^2, \omega_{b2}^2, \ldots, \omega_{bn_b}^2], \tag{68}$$

$$\mathbf{I}_1 = \mathrm{diag}[I_1^{(1)}, I_1^{(2)}, \ldots, I_1^{(N)}], \tag{69}$$

$$\mathbf{a}_0 = [a_0^{(1)}, a_0^{(2)}, \ldots, a_0^{(N)}]^{\mathrm{T}} \tag{70}$$

and

$$\mathbf{b}_0 = [b_0^{(1)}, b_0^{(2)}, \ldots, b_0^{(N)}]^{\mathrm{T}}. \tag{71}$$

6. Generalized forces

Generalized forces of the rotating disk/spindle systems consist of generalized bearing forces, generalized forces from the rotating part, generalized forces from the stationary part, and generalized damping forces. They are described individually as follows.

6.1. Generalized bearing forces

For each bearing, the bearing forces consist of three force components and two moment components. Moreover, the bearing forces are linear combination of spring and damping forces described by

$$\mathbf{F}_b \equiv [F_{xb}, F_{yb}, F_{zb}, M_{xb}, M_{yb}]^{\mathrm{T}} = -\mathbf{K}_b\boldsymbol{\Delta}_b - \mathbf{C}_b\dot{\boldsymbol{\Delta}}_b, \tag{72}$$

where $\mathbf{K}_b$ is the 5×5 stiffness matrix and $\mathbf{C}_b$ is the 5×5 damping matrix.

The virtual work done by the bearing forces is

$$\delta W_b = \sum \mathbf{F}_b^{\mathrm{T}} \delta\boldsymbol{\Delta}_b = -\delta\mathbf{q}^{\mathrm{T}}\mathbf{Q}_b, \tag{73}$$

where the summation sums over all the bearings and $\mathbf{Q}_b$ is the generalized bearing force vector. Substitution of Eqs. (58) and (72) into Eq. (73) yields

$$\mathbf{Q}_b = \mathbf{K}_B\mathbf{q} + \mathbf{H}_B\mathbf{f}_s + \mathbf{C}_B\dot{\mathbf{q}} + \mathbf{G}_B\dot{\mathbf{q}}_s, \tag{74}$$

where

$$\mathbf{K}_B \equiv \sum \mathbf{B}_b^{\mathrm{T}}\mathbf{K}_b\mathbf{B}_b, \quad \mathbf{H}_B \equiv \sum \mathbf{B}_b^{\mathrm{T}}\mathbf{K}_b\mathbf{h}_b, \quad \mathbf{C}_B \equiv \sum \mathbf{B}_b^{\mathrm{T}}\mathbf{C}_b\mathbf{B}_b, \quad \mathbf{G}_B \equiv \sum \mathbf{B}_b^{\mathrm{T}}\mathbf{C}_b\mathbf{h}_b. \tag{75–78}$$

6.2. Generalized forces from rotating part

Let us consider a concentrated load $\mathbf{f}_R$ in the form of

$$\mathbf{f}_R = f_{Rx}\mathbf{I} + f_{Ry}\mathbf{J} + f_{Rz}\mathbf{K}. \tag{79}$$

The load $\mathbf{f}_R$ is fixed in space and acts on a point R on the ith disk. To determine the generalized forces associated with $\mathbf{f}_R$, one needs to determine the displacement $\mathbf{u}_r$ of point R first. According to Fig. 4

$$\mathbf{u}_R = \mathbf{R}_G + (\theta_x\mathbf{i} + \theta_y\mathbf{j}) \times \overrightarrow{GR} + w_i(r_0, \beta_0, t)\mathbf{k}, \tag{80}$$

where $\overrightarrow{GR}$ is the position vector from G to R defined as

$$\overrightarrow{GR} \equiv x_0\mathbf{i} + y_0\mathbf{j} + z_0\mathbf{k} \tag{81}$$

and (r_0, β_0) are the polar co-ordinates of R relative to its disk center C_i. With the assumption of infinitesimal motion, substitution of Eqs. (22) and (25) into Eq. (80) results in

$$\begin{aligned}\mathbf{u}_R = {} & (s_x + R_x + t_z\gamma_y - t_y\gamma_z + z_0\theta_y)\mathbf{I} + (s_y + R_y + t_x\gamma_z - t_z\gamma_x - z_0\theta_x)\mathbf{J} \\ & + \left(s_z + R_z + t_y\gamma_x - t_x\gamma_y - x_0\theta_y + y_0\theta_x + \sum_{m=0}^{\infty}\sum_{n=-\infty}^{\infty} w_{mn}^{(i)}(r_0, \beta_0)q_{mn}^{(i)}(t)\right)\mathbf{K},\end{aligned} \tag{82}$$

or in a matrix form,

$$\mathbf{u}_R = \mathbf{B}_R\mathbf{q} + \mathbf{D}_R\mathbf{f}_s + \sum_{m=0}^{\infty}\sum_{n=-\infty}^{\infty} w_{mn}^{(i)}(r_0, \beta_0)q_{mn}^{(i)}(t)\mathbf{K}, \quad (m, n) \neq (0, 0), (0, \pm 1), \tag{83}$$

where

$$\mathbf{B}_R = \begin{bmatrix} 1 & 0 & 0 & 0 & z_0 & \mathbf{0} & \mathbf{0} & \mathbf{0} & \mathbf{0} \\ 0 & 1 & 0 & -z_0 & 0 & \mathbf{0} & \mathbf{0} & \mathbf{0} & \mathbf{0} \\ 0 & 0 & 1 & y_0 & -x_0 & \mathbf{w}_{00} & \mathbf{w}_{01} & \mathbf{w}_{0,-1} & \mathbf{0} \end{bmatrix}, \tag{84}$$

$$\mathbf{D}_R = \begin{bmatrix} 1 & 0 & 0 & 0 & t_z & -t_y \\ 0 & 1 & 0 & -t_z & 0 & t_x \\ 0 & 0 & 1 & t_y & -t_x & 0 \end{bmatrix}, \tag{85}$$

with

$$\mathbf{w}_{00} \equiv [0 \quad \cdots \quad 0, w_{00}^{(i)}(r_0, \beta_0), 0 \quad \cdots \quad 0]_{(1\times N)}, \tag{86}$$

$$\mathbf{w}_{01} \equiv [0 \quad \cdots \quad 0, w_{01}^{(i)}(r_0, \beta_0), 0 \quad \cdots \quad 0]_{(1\times N)}, \tag{87}$$

$$\mathbf{w}_{0,-1} \equiv [0 \quad \cdots \quad 0, w_{0,-1}^{(i)}(r_0, \beta_0), 0 \quad \cdots \quad 0]_{(1\times N)}. \tag{88}$$

Note that $\mathbf{w}_{00}$, $\mathbf{w}_{01}$, and $\mathbf{w}_{0,-1}$ have zero entries except the ith column.

To obtain the generalized forces, let us consider the virtual work done by $\mathbf{F}_R$ as

$$\delta W_R = \delta \mathbf{u}_R^{\mathrm{T}} \mathbf{f}_R \approx \delta \mathbf{q}^{\mathrm{T}} \mathbf{B}_R^{\mathrm{T}} \mathbf{f}_R + \delta \mathbf{q}_D^{\mathrm{T}} \mathbf{w}_h^{\mathrm{T}} f_{Rz}, \tag{89}$$

where

$$\mathbf{q}_D \equiv [q_{02}^{(i)}(t), q_{03}^{(i)}(t), \ldots, q_{0,-2}^{(i)}(t), q_{0,-3}^{(i)}(t), \ldots]^{\mathrm{T}} \tag{90}$$

and

$$\mathbf{w}_h \equiv [w_{02}^{(i)}(r_0, \beta_0), w_{03}^{(i)}(r_0, \beta_0), \ldots, w_{0,-2}^{(i)}(r_0, \beta_0), w_{0,-3}^{(i)}(r_0, \beta_0), \ldots]. \tag{91}$$

6.3. Generalized forces from stationary part

Let us consider a concentrated load $\mathbf{f}_B$ in the form of

$$\mathbf{f}_B = f_{Bx}\hat{\mathbf{I}} + f_{By}\hat{\mathbf{J}} + f_{Bz}\hat{\mathbf{K}}. \tag{92}$$

The force $\mathbf{f}_B$ is fixed in the shaker frame and acts on a point B on the stationary part. In addition, the position of point B is described by

$$\hat{\mathbf{r}}_B \equiv \overrightarrow{OB} = x_1\hat{\mathbf{I}} + y_1\hat{\mathbf{J}} + z_1\hat{\mathbf{K}}. \tag{93}$$

According to Eqs. (1), (8), and (12), the displacement $\mathbf{u}_B$ of B is

$$\mathbf{u}_B = (s_x + z_1\gamma_y - y_1\gamma_z)\mathbf{I} + (s_y + x_1\gamma_z - z_1\gamma_x)\mathbf{J} + (s_z + y_1\gamma_x - x_1\gamma_y)\mathbf{K} + \sum_{n=1}^{n_b} \mathbf{W}_n(\hat{\mathbf{r}}_B) q_n. \tag{94}$$

Note that small γ_x, γ_y, and γ_z have been assumed to achieve Eq. (94). Moreover, $\mathbf{u}_B$ can be rearranged in a matrix form

$$\mathbf{u}_B = \mathbf{B}_B\mathbf{q} + \mathbf{D}_B\mathbf{f}_s, \tag{95}$$

where

$$\mathbf{B}_B = \begin{bmatrix} 0 & 0 & 0 & 0 & 0 & \mathbf{0} & \mathbf{0} & \mathbf{0} & \mathbf{W}_{Bx} \\ 0 & 0 & 0 & 0 & 0 & \mathbf{0} & \mathbf{0} & \mathbf{0} & \mathbf{W}_{By} \\ 0 & 0 & 0 & 0 & 0 & \mathbf{0} & \mathbf{0} & \mathbf{0} & \mathbf{W}_{Bz} \end{bmatrix}, \tag{96}$$

$$\mathbf{D}_B = \begin{bmatrix} 1 & 0 & 0 & 0 & z_1 & -y_1 \\ 0 & 1 & 0 & -z_1 & 0 & x_1 \\ 0 & 0 & 1 & y_1 & -x_1 & 0 \end{bmatrix}, \tag{97}$$

with

$$\mathbf{W}_{Bx} \equiv [W_{x1}(\hat{\mathbf{r}}_B), W_{x2}(\hat{\mathbf{r}}_B), \ldots, W_{xn_b}(\hat{\mathbf{r}}_B)], \tag{98}$$

$$\mathbf{W}_{By} \equiv [W_{y1}(\hat{\mathbf{r}}_B), W_{y2}(\hat{\mathbf{r}}_B), \ldots, W_{yn_b}(\hat{\mathbf{r}}_B)], \tag{99}$$

$$\mathbf{W}_{Bz} \equiv [W_{z1}(\hat{\mathbf{r}}_B), W_{z2}(\hat{\mathbf{r}}_B), \ldots, W_{zn_b}(\hat{\mathbf{r}}_B)]. \tag{100}$$

Therefore, the virtual work done is

$$\delta W_B = \delta \mathbf{u}_B^{\mathrm{T}} \mathbf{f}_B \approx \delta \mathbf{q}^{\mathrm{T}} \mathbf{B}_B^{\mathrm{T}} \mathbf{f}_B, \tag{101}$$

where the assumption of small γ_x, γ_y, and γ_z is used again.

6.4. Generalized damping forces

The generalized damping forces of the rotating and non-rotating parts can be determined by Rayleigh dissipation function defined as [3]

$$\mathscr{R} = \frac{1}{2} \sum_{i=1}^{N} c_i \int_{A_i} \left(\frac{\mathrm{d}w_i}{\mathrm{d}t} \right)^2 \mathrm{d}A_i + \frac{c_b}{2} \int_V \dot{\mathbf{W}} \cdot \dot{\mathbf{W}} \, \mathrm{d}V, \tag{102}$$

where c_i is the damping coefficient of the ith disk, c_b is the damping of the non-rotating part, and $\mathrm{d}w_i/\mathrm{d}t$ is the material derivative given by

$$\frac{\mathrm{d}w_i}{\mathrm{d}t} = \dot{w}_i(r, \beta, t) + \omega_3 \frac{\partial w_i(r, \beta, t)}{\partial \beta}. \tag{103}$$

With discretizations (8) and (25) and normalizations (10) and (27),

$$\mathscr{R} = \frac{1}{2} \sum_{i=1}^{N} \frac{c_i I_1^{(i)}}{\rho_i h_i} \left[\sum_{m=0}^{\infty} \sum_{n=-\infty}^{\infty} (\dot{q}_{mn}^{(i)} + n\omega_3 q_{m,-n}^{(i)})^2 \right] + \frac{c_b}{2\rho_b} \sum_{n=1}^{n_b} \dot{q}_n^2. \tag{104}$$

The generalized damping forces for the disk are

$$-\frac{\partial \mathscr{R}}{\partial \dot{q}_{mn}^{(i)}} = -\sum_{i=1}^{N} \frac{c_i I_1^{(i)}}{\rho_i h_i} \left[\sum_{m=0}^{\infty} \sum_{n=-\infty}^{\infty} (\dot{q}_{mn}^{(i)} + n\omega_3 q_{m,-n}^{(i)}) \right] \tag{105}$$

and the generalized damping forces for the non-rotating part are

$$-\frac{\partial \mathscr{R}}{\partial \dot{q}_n} = -\frac{c_b}{\rho_b}\sum_{n=1}^{n_b}\dot{q}_n. \tag{106}$$

Therefore, virtual work done by the generalized damping forces is

$$\delta W_d = -\delta \mathbf{q}^{\mathrm{T}}[\mathbf{C}_m\dot{\mathbf{q}} + \mathbf{D}_m\mathbf{q}], \tag{107}$$

where

$$\mathbf{C}_m = \mathrm{diag}[\mathbf{0}, \mathbf{C}_{m22}, \mathbf{C}_{m33}, \mathbf{C}_{m44}, \mathbf{C}_{m55}], \tag{108}$$

with

$$\mathbf{C}_{m22} = \mathbf{C}_{m33} = \mathbf{C}_{m44} = \mathrm{diag}\left[\frac{c_1 I_1^{(1)}}{\rho_1 h_1}, \frac{c_2 I_1^{(2)}}{\rho_2 h_2}, \ldots, \frac{c_N I_1^{(N)}}{\rho_N h_N}\right], \tag{109}$$

$$\mathbf{C}_{m55} = \mathrm{diag}\left[\frac{c_b}{\rho_b}, \frac{c_b}{\rho_b}, \ldots, \frac{c_b}{\rho_b}\right] \tag{110}$$

and

$$\mathbf{D}_m = \begin{bmatrix} \mathbf{0} & \mathbf{0} & \mathbf{0} & \mathbf{0} & \mathbf{0} \\ \mathbf{0} & \mathbf{0} & \mathbf{0} & \mathbf{0} & \mathbf{0} \\ \mathbf{0} & \mathbf{0} & \mathbf{0} & \mathbf{D}_{m34} & \mathbf{0} \\ \mathbf{0} & \mathbf{0} & -\mathbf{D}_{m34} & \mathbf{0} & \mathbf{0} \\ \mathbf{0} & \mathbf{0} & \mathbf{0} & \mathbf{0} & \mathbf{0} \end{bmatrix}, \tag{111}$$

with

$$\mathbf{D}_{m34} = \mathrm{diag}\left[\omega_3\frac{c_1 I_1^{(1)}}{\rho_1 h_1}, \omega_3\frac{c_2 I_1^{(2)}}{\rho_2 h_2}, \ldots, \omega_3\frac{c_N I_1^{(N)}}{\rho_N h_N}\right]. \tag{112}$$

7. Equations of motion

With the kinetic energy, potential energy and generalized forces of the system, one can derive the equations of motion through use of Lagrangian equations. In general, there are two sets of equations of motion. They are described in detail as follows.

The first set of equation couples the rigid-body spindle motion, disk (0,1) modes, disk (0,0) modes, and vibration modes of the stationary part.

$$\mathbf{M}\ddot{\mathbf{q}} + [\mathbf{G} + \mathbf{C}_B + \mathbf{C}_m]\dot{\mathbf{q}} + [\mathbf{K} + \mathbf{K}_B + \mathbf{D}_m]\mathbf{q} = \mathbf{B}_R^{\mathrm{T}}\mathbf{f}_R + \mathbf{B}_B^{\mathrm{T}}\mathbf{f}_B - \mathbf{H}\ddot{\mathbf{f}}_s - \mathbf{G}_B\dot{\mathbf{f}}_s - \mathbf{H}_B\mathbf{f}_s. \tag{113}$$

In Eq. (113), $\boldsymbol{M}$ is the mass matrix defined as

$$\mathbf{M} = \begin{bmatrix} \mathbf{M}_{11} & \mathbf{M}_{12} & \mathbf{M}_{13} & \mathbf{M}_{14} & \mathbf{0} \\ \mathbf{M}_{21} & \mathbf{I}_1 & \mathbf{0} & \mathbf{0} & \mathbf{0} \\ \mathbf{M}_{31} & \mathbf{0} & \mathbf{I}_1 & \mathbf{0} & \mathbf{0} \\ \mathbf{M}_{41} & \mathbf{0} & \mathbf{0} & \mathbf{I}_1 & \mathbf{0} \\ \mathbf{0} & \mathbf{0} & \mathbf{0} & \mathbf{0} & \mathbf{I}_{n_b} \end{bmatrix}, \tag{114}$$

where $\mathbf{I}_1$ is the inertia matrix defined in (69), $\mathbf{I}_{n_b}$ is $n_b \times n_b$ identity matrix,

$$\mathbf{M}_{11} = \mathrm{diag}[M, M, M, \bar{I}_1, \bar{I}_1], \tag{115}$$

$$\mathbf{M}_{21} = \mathbf{M}_{12}^{\mathrm{T}} = [\mathbf{0}_{(N\times 1)}, \mathbf{0}_{(N\times 1)}, \mathbf{I}_1\mathbf{b}_0, \mathbf{0}_{(N\times 1)}, \mathbf{0}_{(N\times 1)}], \tag{116}$$

$$\mathbf{M}_{31} = \mathbf{M}_{13}^{\mathrm{T}} = [\mathbf{0}_{(N\times 1)}, \mathbf{0}_{(N\times 1)}, \mathbf{0}_{(N\times 1)}, \mathbf{0}_{(N\times 1)}, -\mathbf{I}_1\mathbf{a}_0,], \tag{117}$$

$$\mathbf{M}_{41} = \mathbf{M}_{14}^{\mathrm{T}} = [\mathbf{0}_{(N\times 1)}, \mathbf{0}_{(N\times 1)}, \mathbf{0}_{(N\times 1)}, \mathbf{I}_1\mathbf{a}_0, \mathbf{0}_{(N\times 1)}]. \tag{118}$$

Note that $\mathbf{a}_0$ and $\mathbf{b}_0$ used in Eqs. (116)–(118) are defined in Eqs. (70) and (71).

In Eq. (113), $\mathbf{G}$ is a gyroscopic matrix

$$\mathbf{G} = \begin{bmatrix} \mathbf{G}_{11} & \mathbf{0} & -\mathbf{G}_{13} & -\mathbf{G}_{14} & \mathbf{0} \\ \mathbf{0} & \mathbf{0} & \mathbf{0} & \mathbf{0} & \mathbf{0} \\ \mathbf{G}_{31} & \mathbf{0} & \mathbf{0} & 2\omega_3\mathbf{I}_1 & \mathbf{0} \\ \mathbf{G}_{41} & \mathbf{0} & -2\omega_3\mathbf{I}_1 & \mathbf{0} & \mathbf{0} \\ \mathbf{0} & \mathbf{0} & \mathbf{0} & \mathbf{0} & \mathbf{0} \end{bmatrix} \tag{119}$$

with

$$\mathbf{G}_{11} = \bar{I}_3\omega_3 \begin{bmatrix} 0 & 0 & 0 & 0 & 0 \\ 0 & 0 & 0 & 0 & 0 \\ 0 & 0 & 0 & 0 & 0 \\ 0 & 0 & 0 & 0 & 1 \\ 0 & 0 & 0 & -1 & 0 \end{bmatrix}, \tag{120}$$

$$\mathbf{G}_{31} = \mathbf{G}_{13}^{\mathrm{T}} = [\mathbf{0}_{(N\times 1)}, \mathbf{0}_{(N\times 1)}, \mathbf{0}_{(N\times 1)}, 2\omega_3\mathbf{I}_1\mathbf{a}_0, \mathbf{0}_{(N\times 1)}], \tag{121}$$

$$\mathbf{G}_{41} = \mathbf{G}_{14}^{\mathrm{T}} = [\mathbf{0}_{(N\times 1)}, \mathbf{0}_{(N\times 1)}, \mathbf{0}_{(N\times 1)}, \mathbf{0}_{(N\times 1)}, 2\omega_3\mathbf{I}_1\mathbf{a}_0]. \tag{122}$$

In addition, the damping matrices $\mathbf{C}_B$ and $\mathbf{C}_m$ are defined in Eqs. (77) and (108), respectively.

In Eq. (113), the $\mathbf{K}$ is the stiffness matrix from the rotating and non-rotating parts, defined as

$$\mathbf{K} = \mathrm{diag}[\mathbf{0}, \mathbf{I}_1\boldsymbol{\omega}_{00}, \mathbf{I}_1\boldsymbol{\omega}_{01} - \omega_3^2\mathbf{I}_1, \mathbf{I}_1\boldsymbol{\omega}_{01} - \omega_3^2\mathbf{I}_1, \boldsymbol{\omega}_B]. \tag{123}$$

In addition, $\mathbf{K}_B$ and $\mathbf{D}_m$ are defined in Eqs. (75) and (111), respectively.

Finally, the excitation matrix $\mathbf{H}$ in Eq. (113) is defined as

$$\mathbf{H} = \begin{bmatrix} \mathbf{H}_{11} & \mathbf{H}_{12} \\ \mathbf{H}_{21} & \mathbf{H}_{22} \\ \mathbf{0} & \mathbf{0} \\ \mathbf{0} & \mathbf{0} \\ \mathbf{J}_a & \mathbf{J}_a\mathbf{T}_c + \mathbf{J}_b \end{bmatrix}, \tag{124}$$

with

$$\mathbf{H}_{11} = \begin{bmatrix} M & 0 & 0 \\ 0 & M & 0 \\ 0 & 0 & M \\ 0 & 0 & 0 \\ 0 & 0 & 0 \end{bmatrix}, \tag{125}$$

$$\mathbf{H}_{12} = M \begin{bmatrix} 0 & t_z & -t_y \\ -t_z & 0 & t_x \\ t_y & -t_x & 0 \\ 0 & 0 & 0 \\ 0 & 0 & 0 \end{bmatrix}, \tag{126}$$

$$\mathbf{H}_{21} = [\mathbf{0}_{(N\times 1)}, \mathbf{0}_{(N\times 1)}, \mathbf{I}_1\mathbf{b}_0], \quad \mathbf{H}_{22} = [t_y\mathbf{I}_1\mathbf{b}_0, -t_x\mathbf{I}_1\mathbf{b}_0, \mathbf{0}_{(N\times 1)}], \tag{127, 128}$$

$$\mathbf{T}_c = \begin{bmatrix} 0 & t_z & -t_y \\ -t_z & 0 & t_x \\ t_y & -t_x & 0 \end{bmatrix}. \tag{129}$$

Moreover, the excitation matrices $\mathbf{B}_R$, $\mathbf{B}_B$, $\mathbf{G}_B$, and $\mathbf{H}_B$ are defined in Eqs. (84), (96), (78), and (76), respectively.

The second set of equations governs the motion of disk modes with two or more nodal diameters. For the concentrated load applied to the ith disk in the form of Eq. (79), the governing equations are

$$\begin{aligned} &I_1^{(j)}\ddot{q}_{mn}^{(j)} + \frac{c_j I_1^{(j)}}{\rho_j h_j}\dot{q}_{mn}^{(j)} + 2n\omega_3 I_1^{(j)}\dot{q}_{m,-n}^{(j)} + \{[\omega_{mn}^{(j)}]^2 - n^2\omega_3^2\}q_{mn}^{(j)} + n\omega_3\frac{c_j I_1^{(j)}}{\rho_j h_j}q_{m,-n}^{(j)} \\ &\quad = \delta_{ij}W_{mn}^{(i)}(r_0, \beta_0)f_{Rz} \quad j = 1, 2, \ldots, N, \ m = 0, 1, 2, \ldots, \ n = \pm 2, \pm 3, \ldots, \end{aligned} \tag{130}$$

where δ_{ij} is the Kronecker delta.

8. Free and forced response

For free vibration, Eq. (113) can be rearranged as a first order system,

$$\begin{bmatrix} \mathscr{M} & \mathbf{0} \\ \mathbf{0} & \mathbf{I} \end{bmatrix} \begin{bmatrix} \ddot{\mathbf{q}} \\ \dot{\mathbf{q}} \end{bmatrix} = \begin{bmatrix} -\mathscr{C} & -\mathscr{K} \\ \mathbf{I} & \mathbf{0} \end{bmatrix} \begin{bmatrix} \dot{\mathbf{q}} \\ \mathbf{q} \end{bmatrix}, \tag{131}$$

where

$$\mathscr{M} \equiv \mathbf{M}, \quad \mathscr{C} \equiv \mathbf{G} + \mathbf{C}_B + \mathbf{C}_m, \quad \mathscr{K} \equiv \mathbf{K} + \mathbf{K}_B + \mathbf{D}_m. \tag{132–134}$$

Natural frequencies, mode shapes, and damping ratios of the system can be obtained by solving the eigenvalue problem of Eq. (131).

For forced vibration, the transfer functions ($TF\{\cdot\}$) of the system can be obtained as

$$TF\left\{\frac{\mathbf{q}}{\mathbf{f}_R}\right\} = [\mathscr{M}s^2 + \mathscr{C}s + \mathscr{K}]^{-1}[\mathbf{B}_R^{\mathrm{T}}], \tag{135}$$

$$TF\left\{\frac{\mathbf{q}}{\mathbf{f}_B}\right\} = [\mathscr{M}s^2 + \mathscr{C}s + \mathscr{K}]^{-1}[\mathbf{B}_B^{\mathrm{T}}], \tag{136}$$

$$TF\left\{\frac{\mathbf{q}}{\ddot{\mathbf{f}}_s}\right\} = -s^{-2}[\mathscr{M}s^2 + \mathscr{C}s + \mathscr{K}]^{-1}[\mathbf{H}s^2 + \mathbf{G}_B s + \mathbf{H}_B]. \tag{137}$$

When the system is asymptotically stable, frequency response function (FRF) exist and can be obtained by substituting $s = \mathrm{j}\omega$ in Eqs. (135)–(137).

9. Qualitative predictions

When the disks are all identical, it is possible to obtain some qualitative results without explicitly solving Eqs. (113) and (130). To do so, it is necessary to review vibration modes of rotating disk/spindle systems with a rigid base [1].

Basically, the vibration modes are classified into three groups. The first group of modes involves (0,1) disk modes. In this group, rigid-body radial translation and rocking of the spindle are coupled with one-nodal-diameter modes of each disk. When all the disks (say N disks) are identical, the coupled disk/spindle vibration splits into $N-1$ groups of "balanced modes" and a group of "unbalanced modes." For (0,1) unbalanced modes, all the disks vibrate with one nodal diameter in the same phase. As a result of the disk deformation, the inertia force from the left half of the disks is entirely equal and opposite to that from the right half of the disks. These two inertia forces create an unbalanced moment about the centroid. Because the disk/spindle assembly is spinning with an angular momentum about the z-axis, the presence of the unbalanced moment causes the spindle to undergo a steady precession about the Z-axis. For (0,1) balanced modes, two adjacent disks vibrate entirely out of phase, while other disks experience no deformation. Because the out-of-phase vibration does not change the angular momentum, the spindle does not undergo steady precession. As a result, the natural frequencies of the balanced modes are identical to those of the one-nodal-diameter modes of each disk.

The second group of vibration modes involves (0,0) disk modes. In this group, axial translation of the spindle and the (0,0) modes of each disk are couple together. Similarly, the coupled motion split into $N-1$ groups of "balanced modes" and one group of "unbalanced modes." For (0,0) unbalanced modes, all disks undergo the same axisymmetric deformation resulting in an unbalanced inertia force that has to be compensated for by the axial motion of the disk/spindle assembly. By the same token, (0,0) balanced modes have two adjacent disks vibrate entirely out of phase axisymmetrically, while other disks are undeformed.

The third group of vibration modes is disk modes with two or more nodal diameters. For this group of modes, rigid-body translation and rocking of the spindle does not affect disk vibration, because these modes are self-balancing in inertia forces and moments. Response of those modes can be determined through the classical vibration analysis of rotating disks. In other words, when the spindle rotates at constant angular speed ω_3, the pair of (m,n) disk modes will split into two modes with distinct frequencies $\omega_{mn} \pm n\omega_3$ for a ground-based observer.

When flexibility of housing/stator is present, the following qualitative predictions can be obtained from the equations of motion (113) and (130). First, flexibility of the housing/stator will not affect vibration of disk modes with two or more nodal diameters. They will split into two modes with distinct frequencies $\omega_{mn} \pm n\omega_3$ for a ground-based observer. This can be supported by Eq. (130), because Eq. (130) does not contain any parameters from the non-rotating part and takes the same form as in Ref. [1]. Second, flexibility of housing/stator will not affect vibration of balanced (0,0) and (0,1) modes. Physically, balanced modes result from self-balancing of inertia forces and moments. Introduction of housing/stator flexibility does not destroy the self-balancing nature of balanced modes; therefore, balanced modes will remain unaffected. Third, flexibility of housing/stator will couple the (0,1) and (0,0) unbalanced modes through normal modes of the housing/stator as shown in Eq. (113). Finally, base excitations (linear or angular) and external forces acting on the stationary part will not excite balanced modes as well as disk modes with two or more nodal diameters.

10. Experimental studies

Fig. 8 shows the experimental setup. The spindle has ball-bearing supports, and carries two identical disks. The spin speed ranges from 0 to 7200 r.p.m. An automatic impact hammer [28] excites the top disk, and a load cell at the tip of the hammer measures the input force. In the meantime, a fiber-optics laser Doppler vibrometer (LDV) measures vibration of the top disk. The force and velocity signals are fed into a spectrum analyzer, where frequency response functions (FRF) are calculated. Finally, natural frequencies are extracted from the measured FRF.

Four different tests were conducted. The first test is a spindle level test as shown in Fig. 8. In this test, the disk/spindle is mounted on a thick slab of stainless steel, which mimics a rigid housing. In this case, the stationary part is the stator of the spindle motor. The second test is a spindle/base test as shown in Fig. 9. In this case, the disks and spindle motor are mounted on a flexible hard disk drive (HDD) housing, which is bolted to an isolation table. The stationary part is the spindle motor stator plus the base plate. The third and fourth tests are system-level tests as shown in Fig. 10. The system consists of the disks, spindle, base plate, and the top cover. For the third test, the top of the spindle is not attached to the top cover (cf. Fig. 1). In this case, the

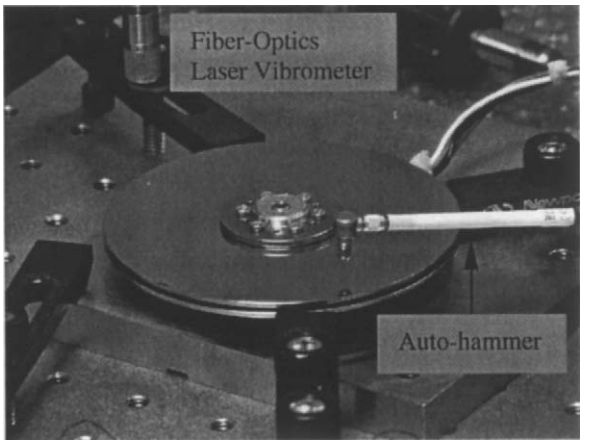

Fig. 8. Experimental setup for ball-bearing spindle; spindle only.

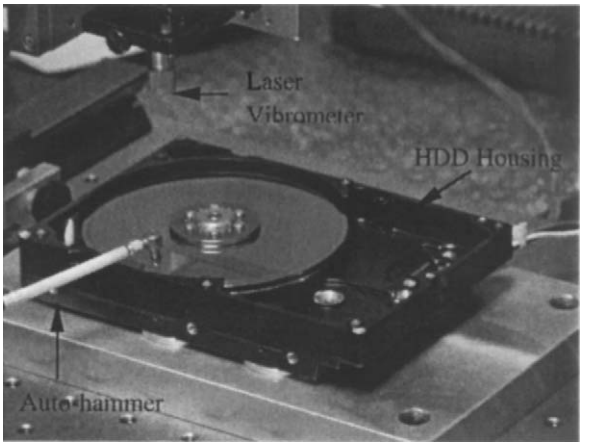

Fig. 9. Experimental setup for ball-bearing spindle; spindle with base.

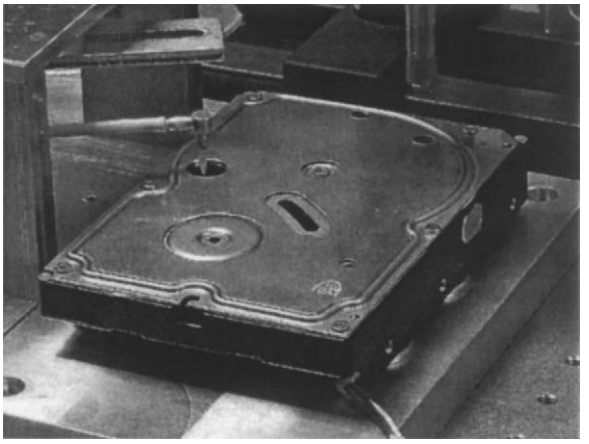

Fig. 10. Experimental setup for ball-bearing spindle; spindle, base, and top.

stationary part is the stator, base, and top without attachment. In the fourth test, the top of the spindle is attached to the top cover via a screw (cf. Fig. 2). In this case, the stationary part is the stator, base plate, and top cover with the stator and the top cover attached together.

These tests have two purposes. The first purpose is to verify the qualitative predictions that the presence of housing/base flexibility does not affect natural frequencies of balanced modes and disk modes with two or more nodal diameters. The second purpose is to compare the measured natural frequencies with numerical predictions to verify the mathematical model. Moreover, comparison of FRF from each test will indicate the effects of base plate, top cover, and top attachment, respectively.

Fig. 11 compares the FRF from the first two tests. The thin line is the FRF of the spindle (with disks), and the thick line is the FRF of the spindle mounted on the base plate. There are three groups of vibration modes. Group I consists of (0,0) balanced mode, (0,1) balanced mode, and (0,2) disk mode. Experimental results in Fig. 11 indicate that presence of the base plate does not affect natural frequencies of these modes. This experimental measurement proves the qualitative prediction that housing/stator flexibility does not affect free vibration of balanced modes and disk modes with two or more nodal diameters. Group II is the (0,1) unbalanced modes in backward and forward precession. The most important phenomenon is mode splitting when the spindle is stationary. When the base plate is not present, the (0,1) forward and backward precessions have the same natural frequency at 0 r.p.m. because the disk/spindle assembly is axisymmetric. When the base plate is introduced, the base plate is rectangular and has different bending stiffness in its two orthogonal principal directions. Therefore, the motor/base configuration no longer has the axisymmetry. In this case, (0,1) forward and backward precession will have different natural frequencies resulting in mode splitting phenomenon. Group III is the (0,0) unbalanced mode. Note that the presence of base plate substantially reduces natural frequency of this mode, because the base plate is soft in bending and allows axial deformation.

Fig. 12 compares the FRF from the second and third tests. The thin line is the FRF of spindle motor with base plate, and the thick line is the FRF of spindle motor with base plate and

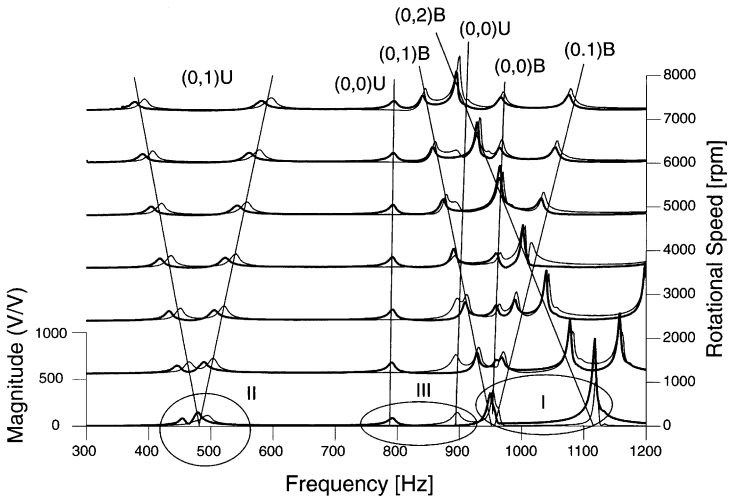

Fig. 11. Experimental results, spindle versus spindle/base; —, spindle only; ——, spindle and base.

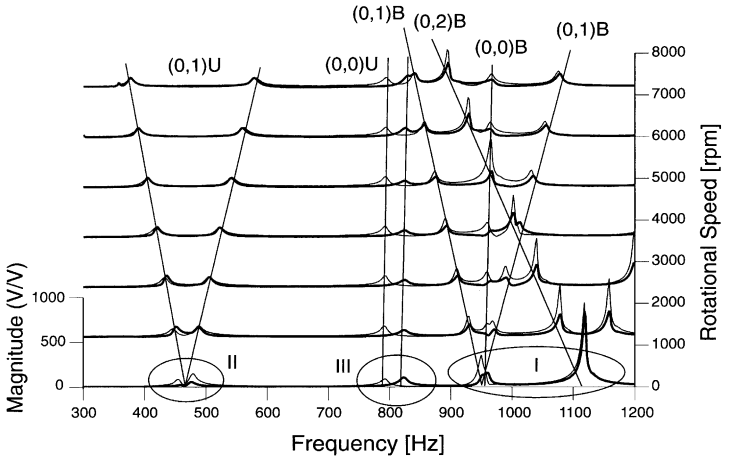

Fig. 12. Experimental results, spindle/base versus spindle/base/top; —, spindle and base; ——, spindle, base, and the top cover (unattached).

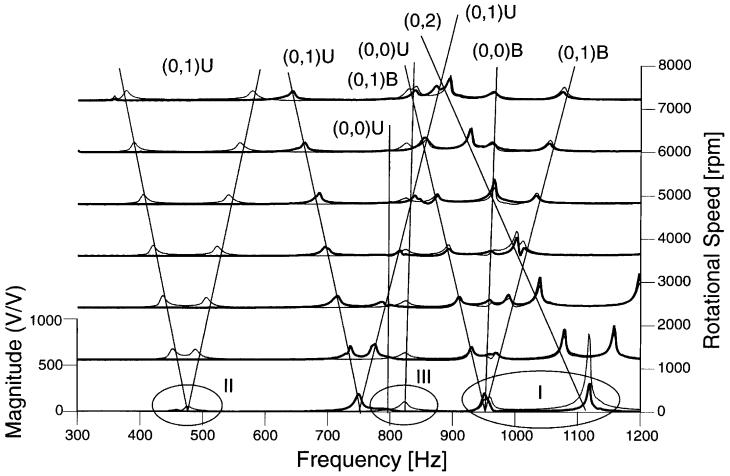

Fig. 13. Experimental results, spindle/base/top, unattached versus attached; —, spindle, base, and the top cover (unattached); ——, spindle, base, and the top cover (attached).

top cover. There are, again, the same three groups of vibration modes. For group I modes, the presence of top cover does not change their natural frequencies, which is in line with the qualitative predictions. Also note that the presence of the top cover substantially reduces the vibration amplitude of group 1 modes when the spindle is rotating. This might come from the confined airflow inside the base plate, when the top cover is introduced. Second, the presence of top cover does not significantly affect the mode splitting of (0,1) unbalanced modes. Third, the presence of top cover increases the natural frequency of (0,0) unbalanced mode, because the top cover contributes to axial stiffness of the system.

Finally, Fig. 13 compares FRF the third and fourth tests. The thin line and thick line represents FRF of unattached and attached systems, respectively. There are three observations. First, the top

attachment does not affect natural frequencies of balanced modes and disk modes with two or more nodal diameters. Second, the top attachment significantly increases the natural frequencies of (0,1) unbalanced modes. Third, the top attachment significantly reduces the amplitude of the amplitude of (0,0) unbalanced mode. This is probably due to the enhanced damping from the constrained layer damping treatment on the top cover.

11. Numerical simulations

The numerical simulation consists of two parts: finite element analysis (FEA) and Matlab simulations. The purpose of the FEA is to calculate natural frequencies ω_{bn}^2 and normalized mode shapes $\mathbf{W}_n(\hat{\mathbf{r}})$ of the stationary part. The purpose of the Matlab simulations is to calculate eigenvalues and eigenvectors of Eq. (131) to predict natural frequencies and mode shapes of (0,1) and (0,0) unbalanced modes. The details of FEA and Matlab simulation are described as follows.

In the FEA, a mesh is first generated on the stationary part. The mesh has solid elements with eight corner nodes, and each node has three degrees of translation and three degrees of rotation. In addition, proper nodal displacements are set to zero to simulate the fixed-end boundary condition in the test. During the FEA, the mode shapes $\mathbf{W}_n(\hat{\mathbf{r}})$ are normalized with respect to the mass matrix. For the stationary parts used in this study (e.g., the HDD base and cover), 100–200 modes are often calculated.

Based on the mode shapes $\mathbf{W}_n(\hat{\mathbf{r}})$ from FEA, the following three sets of data are calculated. The first set of data is $\mathbf{W}_x$, $\mathbf{W}_y$, $\mathbf{W}_z$ defined in Eqs. (61)–(63). This is basically mode shapes evaluated at each bearing, and can be obtained through the three translational nodal displacements from FEA. The second set of data is $\boldsymbol{\alpha}_x$ and $\boldsymbol{\alpha}_y$ defined in Eqs. (64), (65), (39)–(41). Basically, this set of data is the rotation (or slope) of the mode shapes evaluated at each bearing, and it can be obtained through the three rotational nodal displacement from FEA. The third group of data is $\mathbf{J}_{an}$ and $\mathbf{J}_{bn}$ defined in Eqs. (16) and (17).

The natural frequencies and mode shapes obtained from FEA are then used as input to the Matlab program to form the matrices $\mathscr{M}$, $\mathscr{C}$, and $\mathscr{K}$ defined in Eqs. (132)–(134). Solving the eigenvalue problem associated with Eq. (131) then predicts natural frequencies and mode shapes of the complete rotating disk/spindle system coupled with the stationary housing/stator. Furthermore, the Matlab program calculates transfer functions according to Eqs. (135)–(137).

11.1. Natural frequencies

To demonstrate the accuracy of the mathematical model, let us consider the spindle used in Figs. 8–10. Table 1 shows the properties of the rotating part of the spindle. For the disk portion of Table 1, b and a are outer and inner radius of the disk, $I_1^{(i)}$ and $I_3^{(i)}$ are transverse and polar moment of inertia of each disk, m is the mass of the disk, and z_1 and z_2 are the location of the disks relative to the centroid of the rotating part. For the hub portion of Table 1, m_h is the mass of the hub, and I_1^h and I_3^h are the transverse and polar moment of inertia of the hub with respect to the centroid of the rotating part. Finally, z_a and z_b are the location of the two ball bearings relative to the centroid of the rotating part. With the parameters in Table 1, the transverse and

Table 1
Properties of the rotating part of the disk/spindle system used in experiments Figs. 3–5

Disk				Hub		Bearings	
b	47.50 mm	z_1	−0.288 mm	I_1^h	2.712 kg mm^2	z_a	−7.22 mm
a	15.00 mm	z_2	2.682 mm	I_3^h	4.268 kg mm^2	z_b	4.16 mm
$I_1^{(i)}$	13.575 kg mm^2	m	2.260×10^{-2} kg	m_h	2.507×10^{-2} kg		
$I_3^{(i)}$	27.150 kg mm^2						

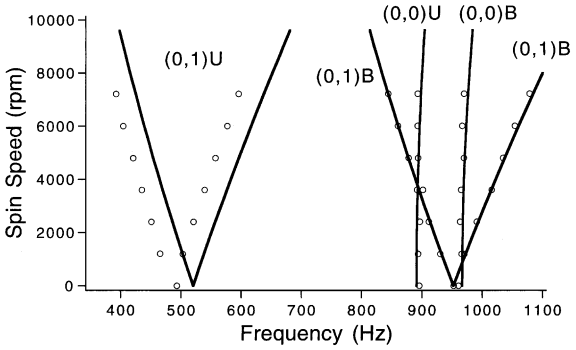

Fig. 14. Comparison of theoretical and experimental results, spindle only; —, theoretical predictions; ◦, experimental measurements.

polar mass moments of inertia of the rotating part with respective to its centroid are $\bar{I}_1 = 30.77$ kg mm^2 and $\bar{I}_3 = 59.62$ kg mm^2, respectively.

The two ball bearings are assumed identical and frictionless. Therefore, $\mathbf{C}_b = \mathbf{0}$. The stiffness coefficients $\mathbf{K}_b$ are obtained through bearing programs [29] as follows:

$$\mathbf{K}_b = \begin{bmatrix} 2.16\times10^7 & 0 & 0 & 0 & -3.47\times10^4 \\ 0 & 2.16\times10^7 & 0 & 3.47\times10^4 & 0 \\ 0 & 0 & 5.76\times10^6 & 0 & 0 \\ 0 & 3.47\times10^4 & 0 & 58.5 & 0 \\ -3.47\times10^4 & 0 & 0 & 0 & 58.5 \end{bmatrix}. \tag{138}$$

In Eq. (138), the unit is in the MKS system.

Fig. 14 compares the theoretical predictions from FEA and Matlab simulation with the experimental measurement for the experimental setup in Fig. 8. The difference between the prediction and experimental results on (0,1) unbalanced modes is about 5%, while other modes are almost perfect match. The 5% difference is unavoidable, because bearing stiffness in Eq. (138) is subjected to several sources of uncertainties. First, bearing components, such as inner race, outer race, and balls, are subjected to manufacturing tolerance. The tolerance will cause variations in the bearing contact angle and subsequently the bearing stiffness. Second, the bearings are glued to the stationary and rotating parts through epoxy. The elasticity of epoxy will also affect the bearing stiffness. Third, the bearing is pre-loaded at an elevated temperature to cure the epoxy.

Therefore, the temperature will also affect the bearing stiffness. All things considered, 5% difference is very insignificant.

Fig. 15 compares the theoretical predictions and the experimental measurements for the setup in Fig. 9. The theoretical results do predict the mode splitting of (0,1) unbalanced modes at 0 r.p.m. Moreover, the difference between the prediction and experimental results on (0,1) unbalanced modes is about 4%. Finally, Fig. 16 compares the theoretical predictions and the experimental measurements for the setup in Fig. 10 with top attachment. The difference between the prediction and experimental results on (0,1) unbalanced modes is about 3%. Also note that the (0,1) and (0,0) unbalanced modes present a curve veering phenomenon [30] as the rotational speed increases from 2000 to 3000 r.p.m.

11.2. Frequency response functions

The mathematical model can predict forced response of spindle systems in terms of frequency response functions (FRF) and time response. Unfortunately, experimental verification for forced response is very difficult. For ball-bearing spindles, bearing damping coefficients in $\mathbf{C}_b$ are not available from any existing theory. Moreover, ball bearings have small damping; therefore, a

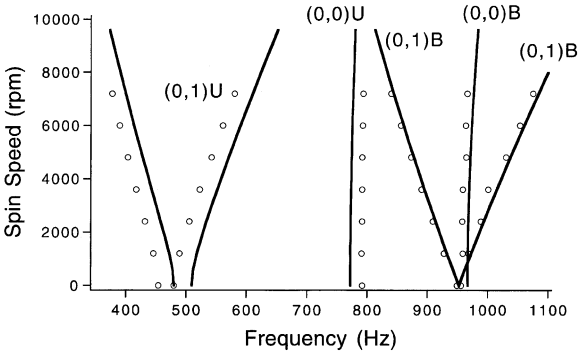

Fig. 15. Comparison of theoretical and experimental results, spindle and base; —, theoretical predictions; ◦, experimental measurements.

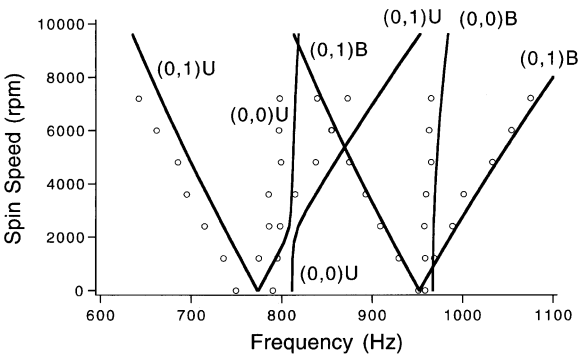

Fig. 16. Comparison of theoretical and experimental results; spindle, base, and top cover with attachment; —, theoretical predictions; ◦, experimental measurements.

slight uncertainty in bearing damping coefficients could lead to very different resonance amplitudes in FRF. Also, it is very difficult to determine the damping coefficients experimentally, because there are too many damping parameters in the $\mathbf{C}_b$ matrix. Therefore, ball-bearing spindles are not ideal for experimental verification. For spindles with hydrodynamic bearings (HDB), the damping coefficients can, in fact, be predicted through use of Reynold's equation. Also, the damping coefficients are much larger than those of the disks, the housing/stator, and the surrounding air. However, prototypes of HDB spindles and their exact parameters are not available at this moment.

Because of the reasons above, this paper will only demonstrate simulated FRF of a virtual spindle with hydrodynamic bearings as follows. The virtual spindle system is identical to the ball-bearing spindle used in the experimental verification, except the bearings are hydrodynamic. Therefore, the stationary part remains the same as in Figs. 8–10. Also, the rotating part has the same parameters as listed in Table 1 except for the bearing locations.

The virtual spindle system has two radial HDB and one thrust HDB. The bearing location and bearing type are listed in Table 2. For radial bearing A, the stiffness matrix has non-zero elements $\mathbf{K}_{b,A}(1,1) = \mathbf{K}_{b,A}(2,2) = 3010.7\omega_3$ and $\mathbf{K}_{b,A}(1,2) = -\mathbf{K}_{b,A}(2,1) = 3196.4\omega_3$. Also, the damping matrix has non-zero element $\mathbf{C}_{b,A}(1,1) = \mathbf{C}_{b,A}(2,2) = 65200$. For radial bearing B, the stiffness matrix has non-zero elements $\mathbf{K}_{b,B}(1,1) = \mathbf{K}_{b,B}(2,2) = 16844\omega_3$ and $\mathbf{K}_{b,B}(1,2) = -\mathbf{K}_{b,B}(2,1) = 34086\omega_3$. Also, the damping matrix has non-zero element $\mathbf{C}_{b,B}(1,1) = \mathbf{C}_{b,B}(2,2) = 69400$. For thrust bearing C, the stiffness matrix has non-zero elements $\mathbf{K}_{b,C}(3,3) = 499390$, $\mathbf{K}_{b,C}(4,4) = \mathbf{K}_{b,C}(5,5) = 0.0015\omega_3$, and $\mathbf{K}_{b,C}(4,5) = -\mathbf{K}_{b,C}(5,4) = 0.000814\omega_3$. Also, the damping matrix has non-zero elements $\mathbf{C}_{b,C}(3,3) = 938.199$ and $\mathbf{C}_{b,C}(4,4) = \mathbf{C}_{b,C}(5,5) = 0.00188$. These non-zero stiffness and damping coefficients are in MKS, and ω_3 is in rad/s.

Since the numerical simulations can consist of various parameter combinations, only the most representative simulated results are illustrated here. Let the X- and Y-axis be along the short and long sides of the stationary part, respectively (e.g., Fig. 9). The excitation conditions are prescribed linear or angular accelerations $\ddot{s}_x(t)$ and $\ddot{\gamma}_y(t)$, which are known through operational tests in the industry. The output location, whose vibration is of interest, is at the top disk with co-ordinates $(x_0, y_0) = (0.045, 0)$ m. The output displacement component is the radial component (i.e., X-component in this case) in the shaker frame. The spin speed is 3000 r.p.m.

Fig. 17 compares FRF of the spindle for three different configurations: spindle motor only, spindle with base and top cover (without top attachment), and spindle with base and top cover (with top attachment). The input excitation is linear acceleration $\ddot{s}_x(t)$. When only the spindle motor is present (i.e., the solid line in Fig. 17), the resonance peaks near 500 Hz correspond to the first pair of (0,1) unbalanced modes. The resonance peaks between 1500 and 2000 Hz correspond

Table 2
Bearing information for the virtual spindle

Bearing number	Bearing type	Location from centroid (mm)
A	Radial	−7.22
B	Radial	4.16
C	Thrust	7.81

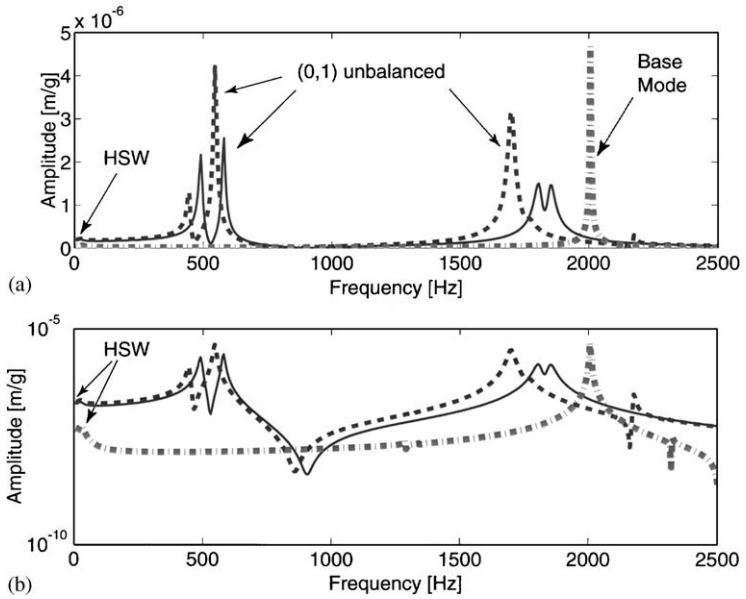

Fig. 17. FRF of the virtual spindle subjected to a linear excitation s_x; (0,1) unbalanced modes; (a) FRF in linear scale, (b) FRF in log scale; —, motor level; - - -, BCU level (motor, base, and cover without attachment); – – –, drive level with attachment.

to the second pair of (0,1) unbalanced modes. When the base and top cover are introduced without attachment (i.e., the dash line labeled BCU in Fig. 17), the flexibility of the stationary part reduces the natural frequencies and increases the resonance amplitudes of (0,1) unbalanced modes. Finally, when the top attachment is added (i.e., the dash-dot line in Fig. 17), the overall FRF amplitude is substantially reduced as indicated in the log-scale plot. Nevertheless, there is a sharp resonance peak at 2000 Hz resulting from a base vibration mode, which has a strong bending motion of the stationary part in the Y (or longitudinal) direction. Because the bearings are hydrodynamic, the bearings respond with a secondary force in the X direction, which is characterized by the off-diagonal terms in the stiffness matrices $\mathbf{K}_{b,A}$ and $\mathbf{K}_{b,B}$. The secondary force subsequently excites the rotating disks and spindle causing significant displacement in the X direction. Fig. 18 zooms in the FRF of Fig. 17 from 0 to 40 Hz. The resonance peak near 25 Hz is the half-speed whirls (HSW). The resonance peak near 2.5 Hz is an axial base mode weakly coupled with the spindle through the thrust bearing. Note that the presence of the top attachment substantially reduces the half-speed whirl.

Fig. 19 compares the FRF of the same three configurations, except that the excitation is the angular acceleration $\ddot{\gamma}_y$. This excitation simulates environments experienced by laptop computers and network storage devices. As opposed to the results in Fig. 17, the angular excitation tends to excite the first pair of (0,1) unbalanced modes much more than the second pair of (0,1) unbalanced modes. Mathematically, this phenomenon can be traced back to Eq. (137). For linear excitations, $\mathbf{G}_B$ and $\mathbf{H}_B$ are zero matrices. For angular excitations, $\mathbf{G}_B$ and $\mathbf{H}_B$ are not zero. Therefore, the presence of non-zero $\mathbf{G}_B$ and $\mathbf{H}_B$ amplifies the response at low-frequency range resulting in larger response for the first pair of (0,1) unbalanced modes.

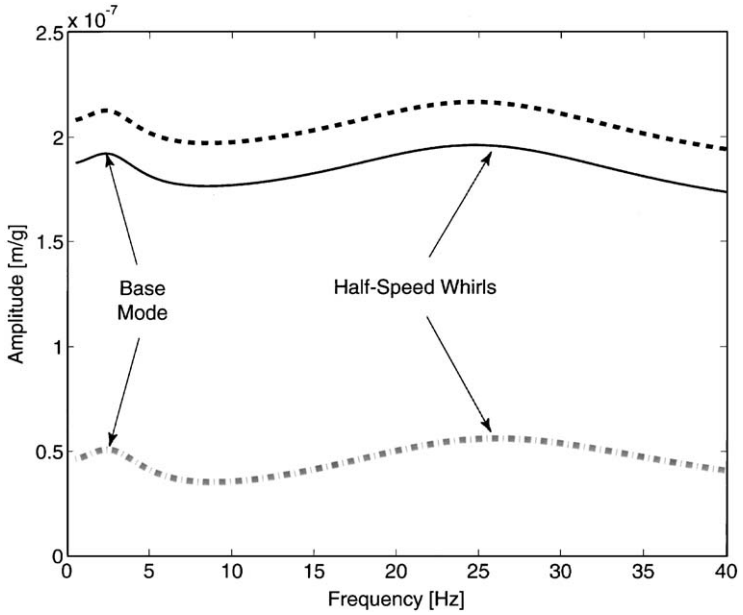

Fig. 18. FRF of the virtual spindle subjected to a linear excitation s_x; half-speed whirls; —, motor level; - - -, BCU level (motor, base, and cover without attachment); – – –, drive level with attachment.

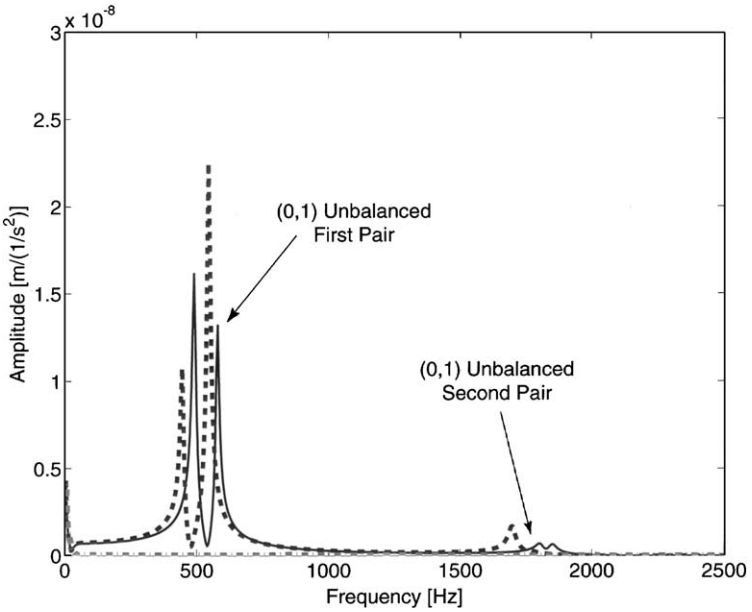

Fig. 19. FRF of the virtual spindle subjected to an angular excitation γ_y; —, motor level; - - -, BCU level (motor, base, and cover without attachment); – – –, drive level with attachment.

12. Conclusions

1. Linearized equations of motion governing vibration of rotating disk/spindle systems mounted on flexible housing/stator assembly are derived through use of Lagrange equation.
2. Flexibility of housing/stator will not affect vibration of disk modes with two or more nodal diameters.
3. Flexibility of housing/stator will not affect vibration of the balanced (0,0) and (0,1) modes.
4. Flexibility of housing/stator will couple the (0,1) and (0,0) unbalanced modes through normal modes of the housing/stator assembly.
5. Base excitations (linear or angular) and external forces acting on the stationary part will not excite balanced modes as well as disk modes with two or more nodal diameters.
6. The mathematical model can predict natural frequencies accurately within 5% of error for ball-bearing spindles.
7. The presence of flexible base and top cover without attachment could reduce natural frequencies and increase the resonance amplitude of (0,1) unbalanced modes.
8. The presence of top attachment substantially reduces the amplitude of (0,1) unbalanced modes and half-speed whirls. Nevertheless, the flexibility of the stationary part could induce larger vibration of a rotating disk/spindle system at other frequencies.
9. Linear base motion tends to excite all (0,1) unbalanced modes equally. In contrast, angular base motion tends to excite the first pair of (0,1) unbalanced modes preferentially.

Acknowledgements

The paper is based on work supported by gifts from Western Digital Corporation and Hitachi Ltd. The authors thank IBM for its support of Mr. Jr-Yi Shen through IBM Cooperative Fellowship.

References

[1] I.Y. Shen, C.-P.R. Ku, A non-classical vibration analysis of multiple rotating disks/shaft assembly, American Society of Mechanical Engineers Journal of Applied Mechanics 64 (1997) 165–174.
[2] I.Y. Shen, Closed-form forced response of a damped, rotating, multiple disk/spindle system, American Society of Mechanical Engineers Journal of Applied Mechanics 64 (1997) 343–352.
[3] C.W. Lee, S.B. Chun, Vibration analysis of a rotor with multiple flexible disks using assumed modes method, American Society of Mechanical Engineers Journal of Vibration and Acoustics 120 (1998) 87–94.
[4] C.W. Lee, J.S, Ham, Mode identification for rotating rigid shaft with flexible disks by mode splits, Journal of Sound and Vibration 225 (1999) 425–446.
[5] R.G. Parker, Analytical vibration of spinning, elastic disk–spindle systems, American Society of Mechanical Engineers Journal of Applied Mechanics 66 (1999) 218–224.
[6] R.G. Parker, P.J. Sathe, Exact solutions for the free and forced vibration of a rotating disk–spindle system, Journal of Sound and Vibration 223 (1999) 445–465.
[7] R.G. Parker, P.J. Sathe, Free vibration and stability of a spinning disk–spindle system, Journal of Vibration and Acoustics 121 (1999) 391–396.
[8] H.S. Jia, On the bending coupled natural frequencies of a spinning, multispan Timoshenko shaft carrying elastic disks, Journal of Sound and Vibration 221 (1999) 623–649.

[9] S. Lim, Finite element analysis of flexural vibrations in hard disk drive spindle systems, Journal of Sound and Vibration 233 (2000) 601–616.
[10] S. Deeyiengyang, K. Ono, Analysis of vibration of hard disk spindle caused by ball bearing, Journal of Information Storage and Processing Systems 3 (2001) 89–99.
[11] J.P. Yang, S.X. Chen, H.C. Chong, Numerical study of dynamic resonance interactions induced by ball bearing defect frequencies, Journal of Information Storage and Processing Systems 3 (2001) 79–87.
[12] S. Deeyiengyang, K. Ono, Suppression of resonance amplitude of disk vibrations by squeeze air bearing plate, IEEE Transactions on Magnetics 37 (2001) 820–825.
[13] T. Jintanawan, I.Y. Shen, C.-P.R. Ku, Free and forced vibration of a rotating disk pack and spindle motor system with hydrodynamic bearings, Journal of Information Storage and Processing Systems 1 (1999) 45–58.
[14] T. Jintanawan, I.Y. Shen, Free vibration of a rotating disk pack and spindle motor system with rotating shaft design, Journal of Information Storage and Processing Systems 2 (2000) 129–139.
[15] T. Jintanawa, I.Y. Shen, K. Tanaka, Vibration analysis of fluid bearing spindles with rotating-shaft design, IEEE Transaction on Magnetics 37 (2001) 799–805.
[16] P.N. Bansal, R.G. Kirk, Stability and damped critical speeds of rotor-bearing systems, American Society of Mechanical Engineers Journal for Industry 97 (1975) 1325–1332.
[17] R. Gash, Vibration of larger turbo-rotors in fluid-film bearings on an elastic foundation, Journal of Sound and Vibration 47 (1976) 53–73.
[18] U.J. Fan, S.T. Noah, Vibration analysis of rotor systems using reduced subsystem models, Journal of Propulsion Power 5 (1989) 602–609.
[19] N.F. Rieger, S. Zhou, An instability analysis procedure for three-level multi-bearing rotor-foundation systems, American Society of Mechanical Engineers Journal of Vibration and Acoustics 120 (1998) 753–762.
[20] L.L. Earles, A.B. Palazzolo, C.K. Lee, C.H. Gerhold, Hybrid finite element–boundary element simulation of rotating machinery supported on flexible foundation and soil, American Society of Mechanical Engineers Journal of Vibration and Acoustics 110 (1988) 300–306.
[21] J.C. Nicholas, L.E. Barrett, The effect of bearing support flexibility on critical speed prediction, ASLE Transactions 29 (1986) 329–338.
[22] R.W. Stephenson, K.E. Rouch, Generating matrices of the foundation structure of a rotor system from test data, Journal of Sound and Vibration 154 (1992) 467–484.
[23] J.A. Vzquez, L.E. Barrett, R.D. Flack, A flexible rotor on flexible bearing supports: stability and unbalance response, American Society of Mechanical Engineers Journal of Vibration and Acoustics 123 (2001) 137–144.
[24] J.G. Tseng, J.A. Wickert, On the vibration of bolted plate and flange assemblies, American Society of Mechanical Engineers Journal of Vibration and Acoustics 116 (1994) 468–473.
[25] J.G. Tseng, J.A. Wickert, Vibration of an eccentrically clamped annular plate, American Society of Mechanical Engineers Journal of Vibration and Acoustics 116 (1994) 155–160.
[26] R.G. Parker, C.D. Mote Jr., Exact perturbation for the vibration of almost annular or circular plates, American Society of Mechanical Engineers Journal of Vibration and Acoustics 118 (1996) 436–445.
[27] R.G. Parker, C.D. Mote Jr., Vibration and coupling phenomena in asymmetric disk-spindle systems, American Society of Mechanical Engineers Journal of Applied Mechanics 63 (1996) 953–961.
[28] H. Bittner, I.Y. Shen, Taming disk/spindle vibrations through aerodynamic bearings and acoustically tuned-mass dampers, IEEE Transaction of Magnetics 35 (1999) 827–832.
[29] A.B. Jones, J.M. McGrew Jr., Rotor-bearing dynamics technology design guide—Part II: ball bearing, Wright Patterson Air Force Aero Propulsion Laboratory, WPAFB, OH, Report No. AFAPL-TR-78-6, 1978.
[30] N.C. Perkins, C.D. Mote Jr., Comments on curve veering in eigenvalue problems, Journal of Sound and Vibration 106 (1986) 451–463.